Enhancing the Performances of Lithium Batteries through Functionalization of Porous Polyolefin Separators with Cross-Linked Single-Ion Polymer Electrolytes

Valentin Vinci, Dimitri Flachard, Helena Henke, Renaud Bouchet, Eric Drockenmuller

Enhancing Performances of Lithium Batteries through Functionalization of Porous Polyolefin Separators with Cross-linked Single-Ion Polymer Electrolytes

Valentin Vinci,[1] Dimitri Flachard,[1,2] Helena Henke,[2] Renaud Bouchet,[1,] and Eric Drockenmuller,[2,*]*

[1] Université Grenoble Alpes, Université Savoie Mont Blanc, CNRS, Grenoble INP, LEPMI, 38000 Grenoble, France

[2] Université Claude Bernard Lyon 1, CNRS, Ingénierie des Matériaux Polymères, UMR 5223, Villeurbanne, F-69622, France

KEYWORDS: lithium-ion batteries, porous polyolefin separators, single-ion polymer electrolytes, cross-linking, surface functionalization.

ABSTRACT: Lithium-ion batteries (LiBs) require advanced separators to meet the growing demands of high energy density, safety, and durability. However, conventional polyolefin separators often suffer from poor electrolyte wettability and limited ionic conductivity, hindering

overall battery performance. This study presents a scalable approach for the surface functionalization of porous polyolefin separators using single-ion statistical copolymers bearing lithium sulfonate or lithium trifluoromethanesulfonamidosulfonyl groups. These copolymers are deposited via a wet-coating process followed by UV cross-linking, achieving durable and uniform functionalization without compromising the separator's porous structure. The functionalized separators exhibit significantly enhanced wettability, electrolyte uptake, and effective ionic conductivity. Electrochemical performance tests of LiBs reveal stable interfacial resistance, improved cycle life, and better rate capabilities owing to the effectiveness of the covalently bonded ionic groups in promoting selective lithium-ion transport. This approach combines simplicity, scalability, and robust chemical stability, offering a promising solution for next-generation LiBs by addressing key limitations of commercial separators.

INTRODUCTION

Lithium-ion batteries (LiBs) have revolutionized portable electronics and are pivotal in the ongoing transition from combustion-based to electrified transportation due to their high energy density and low self-discharge rates.[1–4] Moreover, LiBs are considered as a cornerstone for future large-scale storage of intermittent renewable energy sources.[5–7] These rapidly expanding applications demand enhanced performance, particularly regarding cyclability (>2000 cycles) and power capabilities for fast recharging. A typical LiB comprises three main components: the negative and positive electrodes, which serve as energy reservoirs, and the electrolyte membrane enabling ionic charge transport, typically a liquid electrolyte (LE) absorbed into a porous separator. Most significant improvements in energy density and specific energy are primarily attributed to the development of innovative electrode materials.[8,9] Substantial efforts have also focused on optimizing LE compositions, including tailored mixtures of molecular carbonates (e.g., ethylene

carbonate, propylene carbonate, and dimethyl carbonate) combined with lithium salts such as $LiPF_6$.[10] The separator, a highly porous (over 40% by volume), semi-crystalline polyolefin-based membrane, typically 10–30 μm thick, is a critical component of LiBs.[11–15] While it physically separates the electrodes to prevent short circuits, recent research on functionalized separators highlights their role in enhancing battery performance, reliability, and durability.[16–19] Polyolefin separators are widespread due to their availability, low cost, robust mechanical properties, and (electro)chemical inertness relative to other battery components. In addition, separators should ideally exhibit good wettability and high electrolyte uptake, excellent ionic conductivity, electronic insulation, and excellent thermal stability. The limited wettability of polyolefin-based separators toward polar electrolytes diminishes effective ionic conductivity (σ_{eff}), resulting in uneven current distribution, which undermine LIBs long-term performance and reliability.[20] Indeed, earlier studies reveal that the σ_{eff} of porous separators, once soaked with LE, can decline by 8 to 22-fold compared to the bulk ionic conductivity (σ_0) of the electrolyte.[21–23] The many efforts to enhance σ_0 through LE formulation have only achieved a modest 1.5-fold improvement relative to the EC/DMC-based benchmark electrolyte, LP30 (1M $LiPF_6$).[10,24] The chemical inertness of polyolefins limits the methods available for introducing polar functional groups able to improve wetting, which is critical for enhancing electrolyte uptake, ionic transport, and ultimately the power output and cycle life of LiBs (**Table S1**).

For instance, functionalization methods such as electron beam or plasma-induced polymerizations have enabled the covalent attachment of poly(meth)acrylate chains to the separator surface.[25–28] Coatings based on polydopamine, tannic acid, and cellulose have also improved LE affinity and σ_{eff} through reactive wet coating processes.[29–32] Polydopamine has further been employed as an adhesion layer to anchor additional polymer chains or nanofibers.[33–

[36] Other methods include UV-induced grafting of sulfobetaine-functionalized azides[37] or nitrene-mediated crosslinking of neutral copolymers.[38–41] Physical adsorption techniques, such as dip-coating with copolymers, have also been widely explored.[42–44] Despite observed improvements in wettability and electrolyte uptake, issues like polymer desorption and migration to the electrodes raise concerns about long-term stability. To standardize the assessment of functionalization techniques, a normalized factor (*F*, the ratio of the σ_{eff} of functionalized to pristine separators) has been employed. Most methods yield *F* values between 0.96 and 2.35[28-37,43,44] though higher values (5.6–20.2[26,27,42]) are occasionally reported for separators with initially low σ_{eff} values (**Table S1**). Functionalized separators soaked with LP30 typically show σ_{eff} values between 0.47 and 1.01 mS cm^{-1}, with *F* values in the 1.28-2.35 range. Existing functionalization techniques often rely on complex or poorly controlled processes (e.g., electron-beam irradiation polymerization or dopamine-based coatings) or result in coatings with limited chemical robustness (e.g., physical adsorption by dip coating). Moreover, these methods primarily target wettability improvements without incorporating electrochemically active species, such as single-ion conductors that facilitate Li^+ transport.

To address these limitations, this study proposes a scalable, efficient, and versatile approach for the robust functionalization of polyolefin separators porosity. A series of single-ion statistical copolymers, containing lithium sulfonate or lithium trifluoromethanesulfonamidosulfonyl pendent groups, were synthesized via free radical copolymerization. These copolymers, which also include azidomethyl photo-cross-linkable units and oligo(ethylene glycol)-based comonomers, were deposited on separator surfaces through a wet coating process and cross-linked using UV irradiation. This method bridges the simplicity of physical adsorption with the chemical stability of covalent tethering, achieving uniform functionalization. The coatings were characterized via

scanning electron microscopy with energy-dispersive X-ray spectroscopy (SEM/EDX), and wettability was assessed through contact angle measurements. Electrochemical impedance spectroscopy revealed σ_{eff} improvements across temperature ranges. The influence of copolymer chemical structure on battery performance was systematically investigated in symmetric lithium/lithium cells and lithium/NMC-based batteries, at different *C*-rates and under varied electrolyte excess conditions. The coating of the surface porosity by cross-linked single-ion copolymers is proven to be a general, versatile and efficient way while simple, to improve both battery performance and durability.

EXPERIMENTAL

Materials. Poly(ethylene glycol) methyl ether methacrylate (**1**, PEGMEMA, M_n = 300 g mol^{-1}, $Đ$ = 1.16, ≥ 99%), 1-azidomethyl-4-vinyl-benzene (**2**, 97%), sodium 4-vinylbenzenesulfonate (**3**, > 90%), lithium perchlorate ($LiClO_4$, 99.99%), 2,2′-azobis(2-methylpropionitrile) (AIBN, 98%) and all solvents were purchased from Merck and used as received. Lithium-4-vinyl-*N*-(trifluoromethane)sulfonylbenzene-1-sulfonamide (**4**, STFSILi, 95.2%) and lithium-3-((trifluoromethane)sulfonamidosulfonyl)propyl methacrylate (**5**, MTFSILi, 95.8%) were purchased from Specific Polymers and used as received. Ethylene carbonate (EC, anhydrous, 99%), dimethyl carbonate (DMC, anhydrous, ≥ 99%) and lithium hexafluorophosphate ($LiPF_6$, battery grade, ≥ 99.99% trace metals basis) were purchased from Merck and used as received to prepare a 1:1 (vol/vol) EC/DMC mixture (for contact angle measurements), a 1M solution of $LiPF_6$ in a 1:1 (vol/vol) EC/DMC mixture (known as LP30 standard electrolyte), to perform contact angle measurements and to assemble symmetric stainless-steel cells, symmetric lithium metal cells, and lithium based batteries). Commercial electrodes from NEI Corporation based on

$LiNi_{0.6}Mn_{0.2}Co_{0.2}O_2$ (NMC622) for the positive electrode, and graphite for negative electrode has been used to assemble LIBs. The loading of the positive electrode is 2mAh/cm^2 and the negative to positive ratio is N/P=1.2. A lithium foil from Blue Solutions was used to assemble Li/NMC batteries. Celgard 2400 (**C2400**), a monolayer polypropylene porous separator having a thickness of 25 μm and a porosity of 41 vol% was purchased from MTI Corp and used as received for the assembly of reference Li/Li cells and batteries.

Synthesis of lithium sulfonate–based copolymer 6. A solution of AIBN (37 mg, 0.22 mmol), 1-azidomethyl-4-vinylbenzene **2** (107 mg, 0.67 mmol), 4-vinylbenzenesulfonate **3** (870 mg, 3.8 mmol) in a 1:1 (vol/vol) mixture of water and acetonitrile (10 mL) was degassed by three freeze-pump-thaw cycles before being sealed off under vacuum and stirred for 12 hours at 60 °C. The crude mixture was precipitated in acetone. The resulting material was dissolved in water and precipitated twice in acetone before being dried under vacuum to afford a colorless glassy solid (796 mg, 81.5 %). Part of this sodium-containing copolymer (500 mg, 2.47 mmol) and lithium perchlorate (2.87 g, 27.0 mmol) were dissolved in water (12 mL) and stirred for 12 hours at room temperature. The crude mixture was precipitated in acetone and the cation exchange procedure was repeated twice. Finally, the resulting material was dissolved in water and precipitated twice in acetone before being dried under vacuum to afford **6** as a colorless glassy solid (440 mg, 93.5%). ^{1}H NMR (300 MHz, D_2O): δ 7.63-7.15 (4H, *m*-Ar**H**), 6.80-6.09 (4H, *o*-Ar**H**), 4.38-3.98 (2H, C**H**$_2$N$_3$), 1.98-0.87 (6H, C**H**$_2$CH and CH$_2$C**H**). ^{13}C NMR (400 MHz, D_2O): δ 148.70 (C_1-$Ar_{sulfonate}$), 144.81 (C_1-Ar_{azide}), 140.31 (*p*-C-$Ar_{sulfonate}$), 133.10 (*p*-C-Ar_{azide}), 128.16 (*o,m*-CH-Ar), 125.48 (*o,m*-CH-Ar), 54.03 ($CH_{2,azide}$), 44.26-40.44 ($CH_{2,chain}$, CH_{chain}). ^{7}Li NMR (155.5 MHz, D_2O): δ 0.23 (**Li**).

Synthesis of lithium sulfonate/PEGMEMA-based copolymer 7. A solution of AIBN (450 mg, 2.80 mmol), poly(ethylene glycol) methyl ether methacrylate **1** (2.10 g, 7.00 mmol), 1-azidomethyl-4-vinylbenzene **2** (1.60 g, 10.0 mmol), sodium 4-vinylbenzenesulfonate **3** (7.80 g, 38.0 mmol) in a 1:1 (vol/vol) mixture of water and acetonitrile (100 mL) was degassed by three freeze-pump-thaw cycles before being sealed off under vacuum and stirred for 12 hours at 60 °C. The crude mixture was precipitated in acetone. The resulting material was dissolved in methanol and precipitated in acetone twice before being dried under vacuum to afford a colorless glassy solid (10.1 g, 81.2 %). Part of this sodium-containing copolymer (796 mg, 3.95 mmol) and lithium perchlorate (4.20 g, 39.5 mmol) were dissolved in water (12 mL) and stirred for 12 hours at room temperature. The crude mixture was precipitated in acetone and the cation exchange procedure was repeated twice. Finally, the resulting material was dissolved in methanol and precipitated twice in acetone before being dried under vacuum to afford **7** as a colorless glassy solid (608 mg, 81.7 %). ^{1}H NMR (300 MHz, DMSO-d_6): δ 7.61-7.19 (4H, *m*-Ar**H**), 6.90-6.10 (4H, *o*-Ar**H**), 4.56-4.12 (2H, C**H**$_2$N$_3$), 3.55-3.30 (16H, C**H**$_2$C**H**$_2$O), 3.25-3.18 (3H, C**H**$_3$O), 2.22-0.00 (11H, CH$_2$C(C**H**$_3$), C**H**$_2$C(CH$_3$), C**H**$_2$CH and CH$_2$C**H**). ^{13}C NMR (400 MHz, DMSO-d_6): δ 176.02-174.20 (C=O), 145.15 (C_1-Ar$_{sulfonate}$, C_1-Ar$_{azide}$, p-C-Ar$_{sulfonate}$), 132.94 (*p*-C-Ar$_{azide}$), 126.69-125.72 (*o,m*-CH-Ar), 71.36 (CH$_{2,PEG}$), 69.85 (CH$_{2,PEG}$), 67.96 (CH$_{2,PEG}$), 63.16 (CH$_{2,PEG}$), 58.19 (CH$_{3,PEG}$), 53.56 (CH$_{2,azide}$), 48.75 (C_{chain}), 46.96-43.88 (CH$_{2,chain}$, CH$_{chain}$), 19.54 (CH$_{3,chain}$). ^{7}Li NMR (155.5 MHz, D$_2$O): δ 0.23 (**Li**).

Synthesis of STFSILi/PEGMEMA-based copolymer 8. A solution of AIBN (126 mg, 0.77 mmol), poly(ethylene glycol) methyl ether methacrylate **1** (2.30 g, 7.68 mmol), 1-azidomethyl-4-vinylbenzene **2** (0.92 g, 5.76 mmol) and lithium 4-vinyl-*N*-(trifluoromethane)sulfonylbenzene-1-sulfonamide **4** (8.02 g, 24.96 mmol) in *N*,*N*-dimethylformamide (DMF, 100 mL) was degassed by

three freeze-pump-thaw cycles before being sealed off under vacuum and stirred for 12 hours at 60 °C. The crude mixture was precipitated in ethyl acetate. The resulting material was dissolved in methanol and precipitated twice in ethyl acetate before being freeze dried under vacuum to afford **8** as a white powder (5.86 g, 52.1%). ^{1}H NMR (300 MHz, DMSO-d_6): δ 7.78-7.27 (4H, *m*-Ar**H**), 7.22-6.31 (4H, *o*-Ar**H**), 4.43-4.18 (2H, C**H**$_2$N$_3$), 3.51-3.33 (16H, C**H**$_2$C**H**$_2$O), 3.23-3.14 (3H, C**H**$_3$O), 2.00-0.00 (11H, CH$_2$C(C**H**$_3$), C**H**$_2$C(CH$_3$), C**H**$_2$CH and CH$_2$C**H**). ^{13}C NMR (400 MHz, DMSO-d_6): δ 175.60-173.80 (C=O), 148.17 (C_1-Ar$_{TFSI}$), 144.62 (C_1-Ar$_{azide}$), 142.63 (p-C-Ar$_{sulfonate}$), 132.85 (*p*-C-Ar$_{azide}$), 127.60-126.11 (*o,m*-CH-Ar, CF$_3$), 121.68 (CF$_3$), 118.45 (CF$_3$), 115.23 (CF$_3$), 71.24 (CH$_{2,PEG}$), 69.72 (CH$_{2,PEG}$), 67.84 (CH$_{2,PEG}$), 63.01 (CH$_{2,PEG}$), 58.01 (CH$_{3,PEG}$), 53.41 (CH$_{2,azide}$), 48.41 (C$_{chain}$), 45.76-43.53 (CH$_{2,chain}$, CH$_{chain}$), 19.08-17.59 (CH$_{3,chain}$) ppm. ^{19}F NMR (282.5 MHz, DMSO-d_6): δ –74.95 (s, 3F, C**F**$_3$SO$_2$N) ppm. ^{7}Li NMR (155.5 MHz, CDCl$_3$): δ –0.99 (**Li**).

Synthesis of MTFSILi/PEGMEMA-based copolymer 9. A solution of AIBN (117 mg, 0.71 mmol), poly(ethylene glycol) methyl ether methacrylate **1** (2.14 g, 7.13 mmol), 1-azidomethyl-4-vinylbenzene **2** (0.85 g, 5.35 mmol) and lithium 3-((trifluoromethane)sulfonamidosulfonyl)propyl methacrylate **5** (8.00 g, 23.17 mmol) in DMF (44 mL) was degassed by three freeze-pump-thaw cycles before being sealed off under vacuum and stirred for 12 hours at 60 °C. The crude mixture was precipitated in ethyl acetate. The resulting material was dissolved in methanol and precipitated in ethyl acetate before being dried under vacuum to afford **9** as a white glassy powder (8.48 g, 77.1%). ^{1}H NMR (300 MHz, DMSO-d_6): δ 7.39-6.71 (4H, *m*-Ar**H** and *o*-Ar**H**), 4.44-4.25 (2H, C**H**$_2$N$_3$), 4.15-3.82 (2H, C(O)OC**H**$_2$CH$_2$CH$_2$SO$_2$), 3.57-3.47 (16H, C**H**$_2$C**H**$_2$O), 3.05-2.91 (5H, C**H**$_3$O and C(O)OCH$_2$CH$_2$C**H**$_2$SO$_2$), 2.00-0.00 (15H, C(O)OCH$_2$C**H**$_2$CH$_2$SO$_2$, CH$_2$C(C**H**$_3$), C**H**$_2$C(CH$_3$), C**H**$_2$CH and CH$_2$C**H**). ^{13}C NMR (400 MHz, DMSO-d_6): δ 176.79-175.36 (C=O),

146.55-143.20 (C_1-Ar), 133.12 (*p*-C-Ar), 128.28 (*o,m*-CH-Ar), 124.96 (CF_3), 121.74 (CF_3), 118.52 (CF_3), 115.30 (CF_3), 71.27 ($CH_{2,PEG}$), 69.76 ($CH_{2,PEG}$), 67.81 ($CH_{2,PEG}$), 63.17 ($CH_{2,PEG}$, O-$CH_{2,TFSI}$), 58.02 ($CH_{3,PEG}$), 53.43 ($CH_{2,azide}$), 51.13 (CH_2-SO-), 48.61 (C_{chain}), 44.19 ($CH_{2,chain}$, CH_{chain}), 22.99 (CH_2-*C*H_2-$CH_{2,TFSI}$), 17.69-16.56 ($CH_{3,chain}$). ^{19}F NMR (282 MHz, DMSO-d_6): δ –74.95 (s, 3F, C**F**$_3$SO$_2$N) ppm. ^{7}Li NMR (155.5 MHz, $CDCl_3$): δ –0.98 (**Li**).

General procedure for the functionalization of porous polyolefin separators. A **C2400** separator strip (e.g., 15 × 10 cm^2) was weighed and placed between two polypropylene (PP) layers (**Video S1**). The top PP layer was removed to inject 150 µL of a solution of copolymer **7**, **8** or **9** at a concentration ranging from 1.0 to 6.0 wt% in MeOH. After replacing the top PP layer, the solution was spread over the separator using a glass rod as doctor blade in order to both fill the porosity of the separator and expel the excess of solution. The separator was then dried under vacuum overnight at 30 °C. Finally, each side of the separator was irradiated for 20 minutes at room temperature using a UVACube 400 UV lamp in order to achieve photochemical cross-linking of the copolymer deposited at the surface of the pores. The modified separator was then rinsed in methanol and finally dried overnight at 30 °C under vacuum, before being weighed to quantify the mass of deposited copolymer. For the preparation of functionalized separators with copolymer **6**, 3:1 (vol/vol) mixtures of methanol and water were used.

For all functionalized separators, the weight fraction of copolymer deposited at the surface of the pores (W) was calculated using equation 1:

$$W\ (\%) = 100 \times \frac{w_f - w_i}{w_i} \quad (1)$$

with w_i and w_f the mass of dried separator strips before and after the functionalization process, respectively. An initial kinetic study of the cross-linking reaction by dipping several separators cross-linked at different irradiation times either on one or both sides (**Figure S15**) has shown that

irradiation on both sides resulted in higher *W* values than only one side irradiation for the same cumulated time. UV irradiation for 20 min afforded efficient cross-linking with 100% gel fraction. The theoretical evolution of *W* with the weight fraction of polymer in the coating solution *C* (dashed line in **Figure 1**) is given by equation 2:

$$W_{theo}\ (\%) = 100 \times \frac{m_{\mathrm{p}}}{w_{\mathrm{i}} + m_{\mathrm{p}}} \qquad (2)$$

with w_i the mass of dried separator and $m_p = V_p \times C \times \rho_p$ the mass of deposited copolymer with V_p the porosity volume and $\rho_p = 1.1$ the polymer volumetric mass density.

NMR spectroscopy. ^{1}H NMR (300 MHz) spectra were recorded on a Bruker Avance 300 spectrometer in DMSO-d_6 for **6**, **8**, **9** and D_2O for **7** using hydrogenated solvent residuals as reference (δ = 2.50 and 4.70 ppm, respectively). ^{19}F NMR (282 MHz) spectra of **8** and **9** were recorded on a Bruker Avance 300 spectrometer in DMSO-d_6 using trifluoroethanol as internal reference (δ = –76.76 ppm). ^{7}Li NMR (155.5 MHz) spectra of **6**–**9** were recorded on a Bruker Avance 400 spectrometer in D_2O for **6**, **7** and in DMSO-d_6 for **8**, **9**.

Size exclusion chromatography (SEC) of copolymers **7**, **8** and **9** was performed at 65 °C on a setup comprising a Viscotek TDA max, a Viscotek TDA 305 detector, a Viscotek refractive index detector VE3580, a Viscotek GPC5025 UV detector and a PL 8 µm gel (300 × 8 mm, poly(methyl methacrylate) (A-series)) using DMSO as eluent. The number average molar masses (M_n), the weight average molar masses (M_w) and the chain dispersities ($Đ = M_w/M_n$) were calculated using a refractive index calibration curve obtained from poly(methyl methacrylate) (PMMA) standards.

Differential scanning calorimetry (DSC) was carried out under a 25 mL min^{-1} helium flow with heating and cooling rates of 10 °C min^{-1} in the –120 °C to 130 °C range (higher temperatures induce the thermal cross-linking of the copolymers through thermal decomposition of the azide groups) using a DSC Q200 (TA Instruments). Glass transition temperatures (T_g) of copolymers **6**–

9 were measured at the mid-point of the transition (on the second heating cycle) using the TA Thermal Analysis software.

Thermogravimetric analysis (TGA) measurements were performed under helium using a TGA Q500 (TA Instruments) at a heating rate of 10 °C min^{-1} on copolymers **6**–**9** and **C2400** separator.

Electrolyte uptakes (EU) were performed on **C2400** separator and functionalized separators **C6**–**C9** soaked in LP30 for 12 h at room temperature. Before weighing, the excess liquid electrolyte was removed with a tissue. EU was calculated using equation 3:

$$EU\ (\%) = 100\ \times\ \frac{m_{\mathrm{w}} - m_{\mathrm{d}}}{m_{\mathrm{d}}} \qquad (3)$$

with m_{d} and m_{w} are the mass of the dry and wet separators, respectively.

Contact angle measurements. Contact angles were measured by the sessile drop method on **C2400** separator, on functionalized separators **C6**–**C9**, and on silicon wafers covered with ca. 60 nm thick cross-linked layers of copolymers **6**–**9** (obtained by spin coating a 5.0 wt% solution of copolymer **6** in a 1:3 water/MeOH mixture and 5.0 wt% solutions of copolymers **7**–**9** in MeOH during 30 s at 3000 rpm and 1000 rpm s^{-1}) using an Easydrop contact angle system (KRUSS GmbH, Germany). The wetting liquids were either deionized water, a 1:1 (vol/vol) EC/DMC mixture or LP30. The reported experimental values are averages of at least five measurements taken at room temperature just after deposition of the droplet (V = 1 μL) on different parts of each sample.

Scanning electron microscopy. The morphology of **C2400** separator and functionalized separators **C6**–**C9** were analyzed using a scanning electron microscope (FEG-SEM, Zeiss Ultra 55) with an accelerating voltage of 5 kV. Samples were previously coated with a ca. 1 nm thick palladium/gold sputtered layer. Cross-sections were obtained by cryomicrotomy in liquid nitrogen in the transverse direction of the rolling strip. Scanning electron microscopy/energy dispersive X-

ray spectroscopy (SEM/EDX) analyses were performed using a Brucker Silicon Drift detector in order to either confirm the ion exchange reactions for the synthesis of **6** and **7**, or to confirm the presence of cross–linked copolymers at the center of the separator thickness.

Nitrogen adsorption/desorption measurements were performed on a Micromeritics ASAP 2000 sorption analyzer. Specific surface area (S_{BET}) calculations were made using the Brunauer-Emmett-Teller (BET) method.

Electrochemical impedance spectroscopy (EIS) was performed on symmetric stainless-steel cells in coin cell configuration (**Scheme S1**) comprising a **C2400** separator or functionalized separators **C6**–**C9** soaked by LP30 using a VMP300 multichannel potentiostat (Bio-Logic Science Instruments) with a signal amplitude of 10 to 40 mV in a frequency domain ranging from 1 MHz to 1 Hz. All spectra were first decomposed using an equivalent circuit model based on the impedance of the connections (R_{cables}, inductance cables) in series with an electrolyte resistance (R_{el}) parallel to electrolyte constant phase element (CPE_{el}) circuit, that stands for the soaked separator resistance and pseudo-capacitance, and finally, a pseudo-capacitive CPE element has been added for the two blocking stainless-steel (SS) electrodes. ZView software (Scribner Associates Inc.) was used to fit experimental data. The resistance values (R_{el}) were normalized to the geometrical area of the electrode to calculate the effective conductivity of the soaked separator (σ_{eff}) using equation 4:

$$\sigma_{eff} = \frac{L/S}{R_{el}} \quad (4)$$

with L the sample thickness, S the sample surface and R_{el} the measured resistance.

The ionic conductivity of LP30 as a function of temperature was measured by impedance spectroscopy using a classical conductivity cell (Tacussel) with two platinized platinum parallel electrodes. Prior to the measurements, the cell constant has been determined using a reference KCl

0.1 M aqueous solution at 25 °C. The theoretical effective conductivity of the separators soaked with LP30 (black solid line in **Figure 4**) was calculated, assuming a homogenous dispersion of the pores, using equation 5:

$$\sigma_{eff}^{theo} = \sigma_0 \times \frac{\varepsilon}{\tau} \quad (5)$$

with τ the tortuosity of the separator ($\tau = \varepsilon^{-1.5} = 3.81$ as recently determined by Gasteiger et al.[45]), σ_0 the ionic conductivity of LP30, and ε the porosity of **C2400** ($\varepsilon = 0.41$).

Chronopotentiometry measurements were performed on Li/Li symmetric cells assembled in a glove box in coin cells using either a **C2400** separator or functionalized separators **C6**–**C9**. The Li/Li cells have been cycled at 25 °C in a regulated oven (± 0.1 °C, Memmert IPP30) using a multipotentiostat VMP from Biologic at a current density of ± 50 µA cm^{-2} for 4 hours (i.e., 0.2 mAh cm^{-2}). The time of short-circuit (t_{sc}) is then measured.

Cycling of lithium ion batteries. Galvanostatic cycling with potential limitation (3.0 and 4.2 V for the discharge and charge, respectively) were performed on coin cell batteries assembled in a glove box. The coin cell batteries consist of a NM622 positive electrode ($LiNi_{0.6}Mn_{0.2}Co_{0.2}O_2$, provided by NEI) with a loading of 2.0 mAh cm^{-2}, and either a negative lithium metal electrode (50 µm thick, provided by Blue Solutions) or a Graphite electrode with a loading of 2.4 mAh cm^{-2} (provided by NEI), and either a **C2400** separator or functionalized separators **C6**–**C9** soaked by LP30 (**Scheme S1**). The electrochemical performances were determined at 25 °C and at *C* rates ranging from *C*/10 to 3*C*.

Scheme 1. Chemical Structures of Lithium–Containing Single–Ion Statistical Copolymer Electrolytes 6-9.

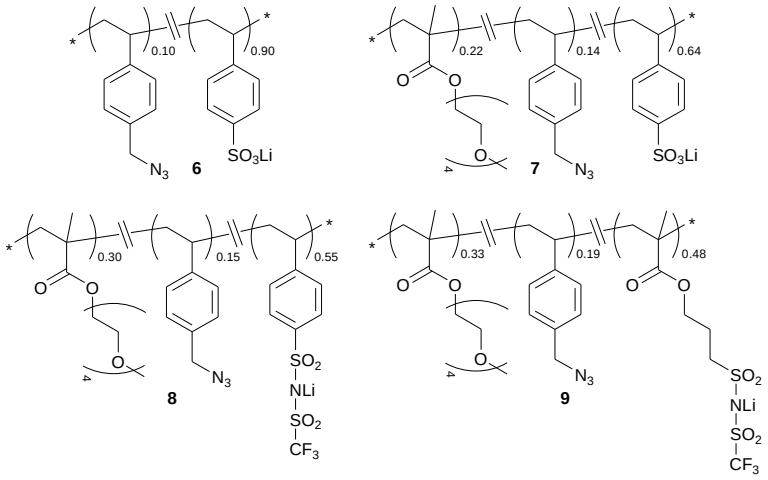

RESULTS

Synthesis and Characterization of Statistical Copolymers 6–9. Single-ion lithium-containing statistical copolymers **6–9** were synthesized by free radical solution copolymerization using AIBN as an initiator (**Schemes 1** and **S2**). They incorporate azidomethyl pendant groups (10–19 mol%), enabling solid-state cross-linking and surface tethering through highly reactive nitrene intermediates generated under UV irradiation at 365 nm (**Scheme S3**).[39–41]

Lithium sulfonate-containing copolymers **6** and **7** were synthesized in two steps: free radical copolymerization in a 1:1 (vol/vol) water/acetonitrile mixture followed by three successive ion exchange reactions with aqueous $LiClO_4$ to introduce lithium counter-cations. SEM-EDX analysis of dense membranes of copolymers **6** and **7**, conducted before and after ion exchange, confirmed quantitative lithium cation incorporation by the disappearance of the sodium peak at 1.04 keV (e.g., **Figure S1** for **6**). Their chemical structures were confirmed by ^{1}H, ^{13}C and ^{7}Li NMR spectroscopy (**Figures S2–S6**). Integration of ^{1}H NMR spectra revealed the compositions of copolymers **6** (10 mol% azidomethyl and 90 mol% lithium sulfonate units) and **7** (14 mol%

azidomethyl, 64 mol% lithium sulfonate and 22 mol% monomethoxy–oligo(ethylene glycol) units, **Table S2**). Copolymers **6** and **7** exhibited limited solubility (**Table S3**): insoluble in common organic solvents such as heptane ($n$$C_7H_{16}$), ethyl acetate (EtOAc), acetone, diethyl ether (Et_2O), tetrahydrofuran (THF), dichloromethane (CH_2Cl_2), chloroform ($CHCl_3$), acetonitrile (CH_3CN), toluene ($PhCH_3$), and a 1:1 (vol/vol) EC/DMC mixture. However, they dissolved in water and dimethylformamide (DMF) at 10 mg mL^{-1}. Additionally, copolymer **7**, containing hydrophilic PEGMEMA units (22 mol% or 31 wt%), was also soluble in methanol (MeOH) and dimethylsulfoxide (DMSO), unlike copolymer **6**. Copolymers **8** and **9** were synthesized in a single step by free radical copolymerization in DMF, using PEGMEMA **1**, 1-azidomethyl-4-vinylbenzene **2**, and either styrenic or methacrylic lithium (trifluoromethyl)sulfonamidosulfonyl monomers **4** and **5**, respectively. Their structures were validated by ^{1}H, ^{13}C ^{7}Li, and ^{19}F NMR spectroscopy (**Figures S6–S11**). Molar ratios of 30:15:55 for monomers **1**/**2**/**4** in copolymer **8** and 33:19:48 for monomers **1**/**2**/**5** in copolymer **9** were obtained via ^{1}H NMR analysis, showing significant composition drift from the initial monomer feed (20:15:65 for both mixtures). The (trifluoromethyl)sulfonamidosulfonyl (TFSI) anion, with its enhanced charge delocalization and ion-pair solvation, significantly expanded the solubility range of copolymers **8** and **9** compared to their lithium sulfonate counterparts. Like **6** and 7, copolymers **8** and **9** were insoluble in $n$$C_7H_{16}$, EtOAc, Et_2O, CH_2Cl_2, $CHCl_3$, and $PhCH_3$, while soluble in water and DMF at 10 mg mL^{-1}. Due to the presence of PEGMEMA units, they also dissolved in MeOH and DMSO. Furthermore, the TFSI anion enabled solubility in acetone, THF, CH_3CN, and notably in a 1:1 EC/DMC mixture and LP30, making them suitable for use in electrochemical cells and batteries (**Table S3**). Size exclusion chromatography (SEC) analysis of copolymers **7–9** (**Figure S12**), using DMSO as the eluent, revealed relatively high molar masses (M_n =120, 172, and 183 kg mol^{-1} for **7**, 8, and **9**,

respectively, based on PMMA standards) and dispersities ($Đ$ =4.9, 2.2, and 3.1, respectively). These relatively high dispersity values are likely due to interactions between polymer chains and the stationary phase during SEC elution.

The thermal properties of copolymers **6–9** were analyzed using differential scanning calorimetry (DSC) and thermogravimetric analysis (TGA). Notably, no glass transition temperature (T_g) was observed for copolymers **6** and **7** within the -100 - 120 °C range. At higher temperatures, a cross-linking reaction may occur due to the thermal decomposition of azide units, which starts around 150 °C depending on the heating rate. Thermal degradation of these copolymers occurs at even higher temperatures, before any evidence of T_g transition (**Figure S13**). The absence of a T_g for copolymers **6** and **7** is characteristic of water-soluble polycations and polyzwitterions with poorly delocalized ion pairs.[46] In contrast, copolymers **8** and **9** are amorphous materials with T_g values of 65 °C and 43 °C, respectively, displaying the glassy behavior typical of poly(ionic liquid)s, which are polymer electrolytes with highly delocalized ion pairs.[47] These experimentally determined T_g values align well with predictions from Fox's law (T_g = 62 °C and 36 °C for **8** and **9**, respectively), calculated using molar ratios determined via ^{1}H NMR spectroscopy and T_g values of the corresponding homopolymers (T_g = -56 °C, 102 °C, 152 °C, and 95 °C for homopolymers of **1**, **2**, **4**, and **5**, respectively).[48–51] Thermal stability of copolymers **6–9** was further evaluated using TGA (**Figure S14**). Copolymers containing lithium sulfonate (**6** and **7**) exhibited greater thermal stability than those with lithium TFSI (**8** and **9**), with temperatures at 10 wt% loss (T_{d10}) of 390 °C, 350 °C, 295 °C, and 260 °C, respectively. However, due to the structural complexity of these statistical copolymers-comprising mixtures of two or three comonomers with varying chemical and physical properties, as well as composition drifts inherent to free radical copolymerization, the specific chemical degradation events (e.g., cleavage of ester and ether side groups, backbone

scission) were not examined in detail. Notably, the char residue content at 600 °C also varied significantly between the two series, with values of approximately 57 wt% and 54 wt% for copolymers **6** and **7**, compared to 8 wt% and 10 wt% for copolymers **8** and **9**, respectively. The T_{d10} values of copolymers **6–9** are however significantly higher than the operating temperature range of LiBs and exceed those of the C2400 separator (T_{d10}= 280 °C).

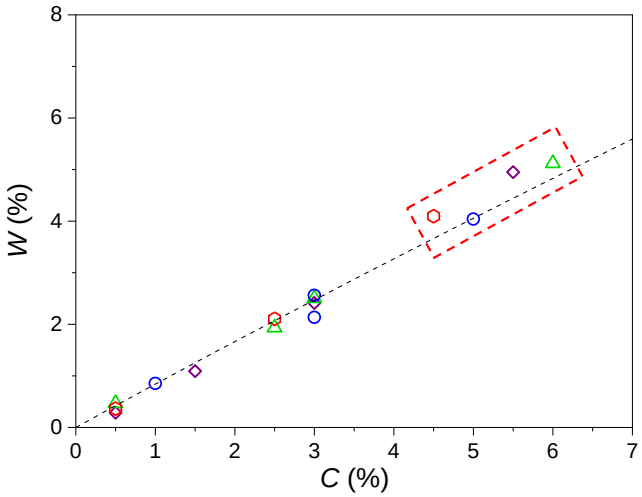

Figure 1. Weight fraction (W) of copolymers deposited at the surface of the **C2400** separator pores as a function of the weight fraction of copolymers in the coating solution (C) for lithium–containing single–ion copolymer electrolytes **6** (open purple diamonds), **7** (open green triangles), **8** (open red hexagons) and **9** (blue open circles); the grey dashed line represents the theoretical evolution calculated with equation **2**. Samples further characterized and used for the preparation of electrochemical cells are designated by the red dashed rectangle.

Surface Functionalization of Porous Separators. The surface functionalization of a porous commercial Celgard separator (**C2400**) was achieved through a two-step process: (**i**) wet coating

of the separator pores with solutions of copolymers **6–9** (**Video S1**) and (**ii**) solid-state cross-linking of the deposited copolymers via UV irradiation. Methanol was employed as the solvent for the deposition of copolymers **7–9**, as it both solubilizes the copolymers and ensures effective wetting of the **C2400** separator. For copolymer **6**, a 1:1 (vol/vol) methanol/water mixture was used due to its insolubility in pure methanol. Cross-linking conditions were optimized using copolymer **8** (**Figure S15**). For the chosen setup—defined by the intensity of the UV lamp and the sample distance—20 minutes of irradiation per side (cumulative irradiation time of 40 minutes) ensured 100% retention of the deposited copolymer after soaking in a good solvent. This duration allowed sufficient UV penetration and achieved homogeneous cross-linking throughout the sample thickness. In the studied concentration range (0.5–6.0 wt%), a linear relationship was observed between the weight fraction of deposited copolymer (*W,* equation **1**) and the weight fraction of copolymer in the coating solution (*C*) (**Figure 1**). However, at higher concentrations (*C* = 10–50 wt%), deviations from linearity were evident. These deviations were associated with the formation of non-porous skin layers on the separator surface and clogging of the pores, which compromised separator functionality. For subsequent studies, separators (**C6–C9**) with *W* values in the range of 4.0–5.0 wt% (highlighted in the red dashed rectangle in **Figure 1**) were selected for further characterization and testing.

Wettability and Electrolyte Uptake. The wettability of the **C2400** separator, functionalized separators **C6–C9**, and cross-linked thin films of copolymers **6–9** (ca. 60 nm thick, spin-cast on silicon wafers) was evaluated using static contact angle measurements with H_2O, a 1:1 (vol/vol) EC/DMC mixture, and LP30 as liquid probes (**Table 1**, **Figure 2**, **Figure S16**). Among all tested samples, the unmodified **C2400** separator exhibited the highest contact angles (θ): 127° for H_2O, 57° for EC/DMC, and 95° for LP30. For the **C6–C9** separators, θ values decreased with increasing

W. At *W* values of 4.0–5.0 wt%, θ values ranged from 88–103° for H_2O, 40–46° for EC/DMC, and 61–65° for LP30, aligning with literature-reported values for wetting of liquid probes on both pristine and functionalized polyolefin separators (**Table S1**).[29-31,33,35-37] Interestingly, cross-linked thin films of copolymers **6–9** exhibited much lower θ values: 30–35° for H_2O, 10–12° for EC/DMC, and 19–26° for LP30. These differences can be attributed to the Cassie-Baxter wetting effect caused by the surface roughness of the porous separators, as commonly observed for textured materials.[52] Electrolyte uptake (EU) of LP30 was also measured (equation 3**, Table 1**) for the **C2400** and **C6–C9** separators. As expected, and in agreement with literature,[26,27,29-37,43,44] the functionalized separators exhibited higher EU values than the unmodified **C2400** separator due to their improved wettability (**Figure S17**). The measured EU values (ranging from 108% to 136%) are consistent with the porosity of the **C2400** separator and the absence of swelling by the electrolyte, further validating the effectiveness of the functionalization process.

Table 1. Physical properties of the **C2400** separator and functionalized separators **C6-C9**.

N°	Copolymer	*W* [wt%][a]	*EU* [%][b]	Contact Angle [°][c]			S_{BET} [m² g^{-1}][d]	σ_{eff} [mS cm^{-1}][e]	*F*[f]
				H_2O	EC/DMC	LP30			
C2400	/	0	88	127	57	95	42	0.24	1
C6	**6**	5.0	108	90	42	65	107	0.71	3.0
C7	**7**	5.1	122	103	41	65	35	0.90	3.8
C8	**8**	4.1	133	88	46	63	32	0.99	4.1
C9	**9**	4.0	136	90	40	61	36	0.98	4.1

[a]Determined by gravimetry; [b]Determined by gravimetry after soaking with LP30; [c]Determined by the sessile drop method; [d]Determined from N_2 adsorption/desorption isotherms; [e]Determined by EIS at 25 °C after soaking with LP30; [f]Ratio between the effective conductivities of the functionalized separators **C6**–**C9** and the **C2400** separator soaked with LP30.

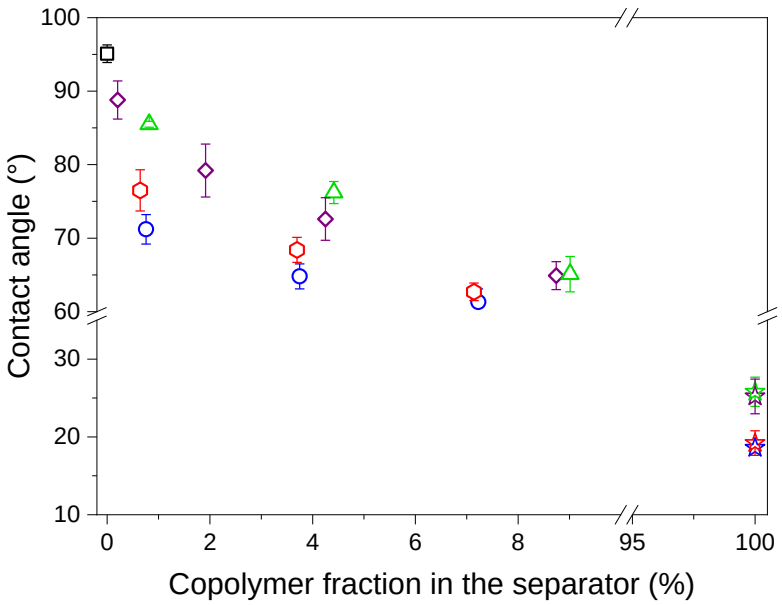

Figure 2. Contact angles of LP30 on **C2400** (open black square), on functionalized separators **C6** (open purple diamonds), **C7** (open green triangles), **C8** (open red hexagons) and **C9** (open blue circles) for different contents of deposited copolymers **6-9**, and on ca. 60 nm thick cross-linked layers of copolymers **6** (open purple star), **7** (open green star), **8** (open red star) and **9** (open blue star) spin coated on silicon wafers.

Morphology of the Porous Separators. The morphology and chemical composition of the **C2400** separator and functionalized separators **C6–C9** were characterized using SEM and SEM/EDX analyses (**Figure 3**, **Figures S18–S22**). The pristine **C2400** separator displayed uniform elongated pores, formed by an interconnected network of thin fibrils and thicker perpendicular fibrils, oriented relative to the separator's rolling direction (**Figure 3**, **Figure S18**). Upon functionalization, the separators exhibited distinct morphological changes, depending on the

copolymer used. Compared to **C2400**, SEM images of **C6** and **C7** revealed irregularly shaped ovoid pores and spherical aggregates (~120 nm in diameter) for **C6**, as well as thicker, aggregated and distorted fibril structures together with the presence of perpendicular microfibrils for **C7** (**Figures 3**, **S19** and **S20**). Conversely, functionalized separators **C8** and **C9** showed relatively uniform morphology, characterized by thick, straight fibrils with a few smaller perpendicular fibrils, likely composed of cross-linked copolymers **8** and **9** (**Figure 3**, **Figures S21** and **S22**).

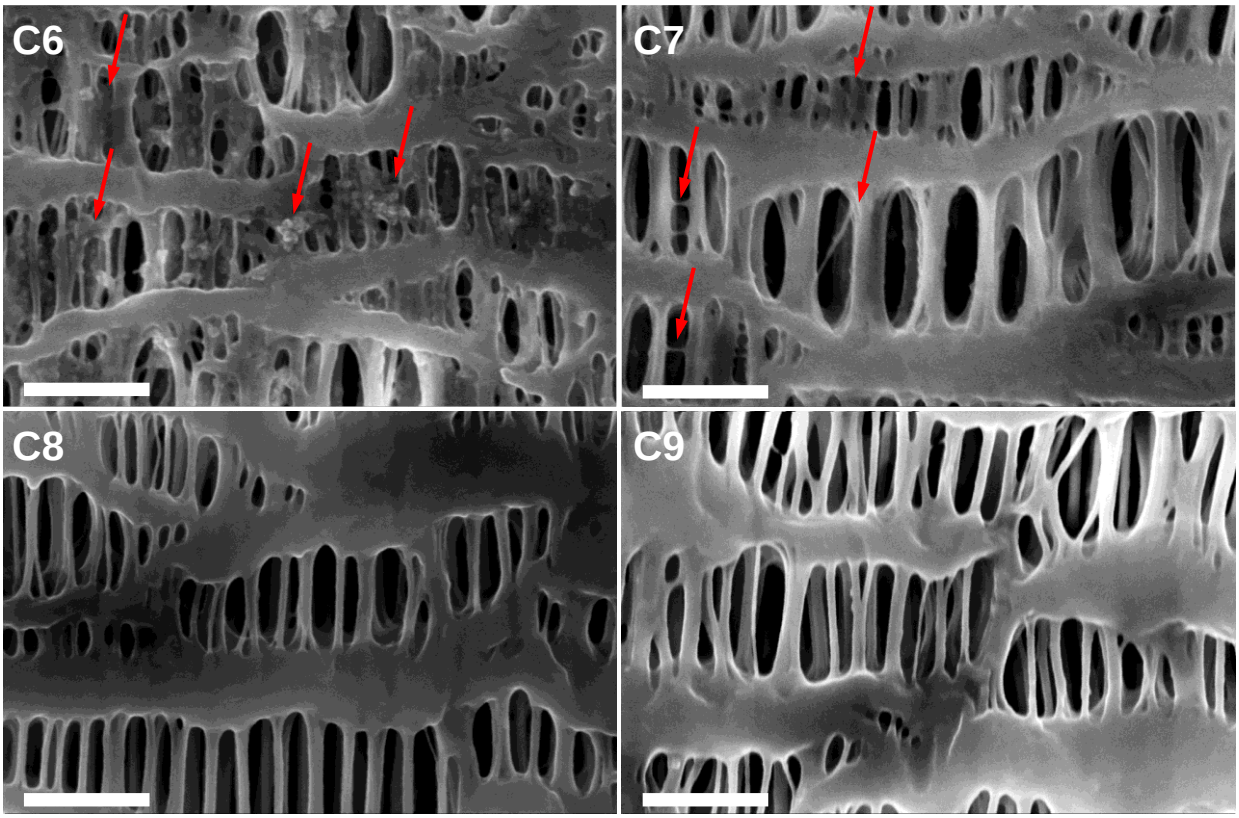

Figure 3. SEM images of the surface of functionalized separators **C6**–**C9** (white bars = 500 nm). The red arrows highlight the presence of spherical aggregates, aggregated fibrils and perpendicular microfibrils.

Cross-sectional SEM images confirmed that the porosity (i.e., pore number, size, and connectivity) of **C2400** remained largely unchanged after the functionalization process, indicating the deposition did not compromise the separator's porous structure. SEM/EDX analyses of the cross-sectional areas (highlighted in red squares in **Figures S19–S22**) confirmed the uniform distribution of copolymers **6–9** throughout the separator thickness. This was evidenced by the detection of sulfur (2.3 keV) and, for copolymers **8** and **9**, fluoride (0.6 keV) peaks in functionalized separators, which were absent in the pristine **C2400** separator (**Figure S18**). Nitrogen adsorption/desorption isotherms were used to calculate specific surface areas (S_{BET}) of the separators according to the Brunauer-Emmett-Teller (BET) method (**Figure S23**). The unmodified **C2400** separator exhibited an S_{BET} of 42 $m^2\ g^{-1}$.[53] Functionalized separator **C6** showed a significantly higher S_{BET} of 107 $m^2\ g^{-1}$, consistent with SEM observations of spherical aggregates on its surface. Conversely, separators **C7–C9** exhibited S_{BET} values close to that of the pristine **C2400** separator (35–42 $m^2\ g^{-1}$), indicating thin and homogeneous copolymer layers deposited on the pores surface.

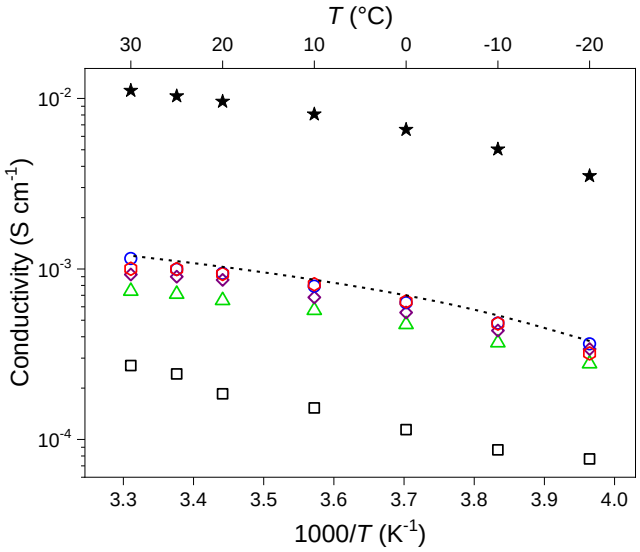

Figure 4. Effective ionic conductivities (σ_{eff}) of the **C2400** separator (solid black squares) and functionalized separators **C6** (open purple diamonds), **C7** (open green triangles), **C8** (open red

stars) and **C9** (open blue circles) soaked with LP30. Bulk ionic conductivity (σ_0) of LP30 (dashed black line) and theoretical effective ionic conductivity (σ_{eff}^{theo}) values for **C2400** soaked by LP30 calculated using equation **5** (dashed black line).

Ionic Conductivity. The effective ionic conductivities (σ_{eff}) of the **C2400** separator and functionalized separators **C6–C9** soaked with LP30 were evaluated and presented in Arrhenius coordinates in **Figure 4**. The ionic conductivity of LP30 (σ_0 = 10.3 mS cm^{-1} at 25 °C) aligns well with reported literature values.[10,14,24] σ_{eff}^{theo} of the **C2400** separator soaked with LP30 can be estimated using equation 4. However, accurate experimental determination of the tortuosity (τ) of untreated polyolefin separators like **C2400** is challenging due to their poor wettability with the LE (see **Table 1**).[21-23] Literature values for τ of various commercial polyolefin separators (e.g., Celgard 2325, 2400, 2500, and Solupor 14P01A, 3P07A, 10P05A) soaked with LP30 range widely from 4 to 14.[10,21,23] These values significantly exceed the theoretical tortuosity predicted by the Bruggemann law ($\tau = \varepsilon^{-\alpha} = 1.35$ with ε the porosity and $\alpha = 0.5$ for an assembly of insulating spheres).[54] Recent studies by Gasteiger et al. demonstrated that such separators follow a modified Bruggemann law ($\tau = \varepsilon^{-1.5}$).[45] Using a porosity of $\varepsilon = 0.41$ for **C2400**, a tortuosity of 3.81 is estimated, yielding σ_{eff}^{theo} = 1.11 mS cm^{-1} at 25 °C. Experimentally, however, σ_{eff} of the **C2400** separator at 25 °C was measured to be 0.24 mS cm^{-1}, which is approximately 43-fold lower than σ_0 of LP30 and nearly 5-fold lower than σ_{eff}^{theo} (**Figure 4**). This significant reduction in σ_{eff} is attributed to the poor wettability of the separator, leading to incomplete pore filling, reduced effective porosity, and increased apparent tortuosity (cf. Bruggemann law). Enhancing the wettability and electrolyte uptake of the separator is thus critical to improve σ_{eff}. Functionalized separators **C6–C9**, owing to their superior wettability, exhibit σ_{eff} values ranging from 0.71 to 0.99 mS cm^{-1}, which is significantly higher than for the pristine **C2400** separator. Correspondingly, the

effective tortuosity (τ_{eff}) decreases from 17.7 (pristine **C2400**) to as low as 4.3 for functionalized separators **C8** and **C9**. The σ_{eff} values for **C8** and **C9** are among the highest reported in the literature and are in excellent agreement with theoretical estimates, indicating these systems have reached the highest theoretical ionic conductivity. The lower σ_{eff} values observed for **C6** and **C7** are likely due to less uniform coatings (as evidenced by SEM, **Figure 3**) and the lower solvation and swelling ability of lithium sulfonate–based layers in LP30. In contrast, separators **C8** and **C9** benefit from the solvation of grafted TFSI-Li moieties by LP30, providing additional free Li^+ ions (approximately 0.15 mol L^{-1}, based on the copolymer weight fraction and residual pore volume). This excess Li^+ not only enhances the wetting of the separator but also contributes to the measured σ_{eff} further improving ionic conductivity. Consequently, the enhanced ionic conductivity of **C8** and **C9** separators is expected to positively impact lithium-ion battery (LiB) performance.

Electrochemical characterization of lithium/lithium symmetric cells. Galvanostatic cycling measurements at ±50 μA cm^{-2} were conducted on symmetric Li/Li cells using either the **C2400** separator or functionalized separators **C6–C9**. Each cycle lasted 4 hours (**Figure 5**). Lithium metal stripping/plating in Li/Li symmetric cells is highly sensitive to current density distribution, making this a precise method for evaluating the homogeneity of separator wetting.[55] The figure of merit for separators is assessed by measuring the number of exchanged coulombs before a short circuit occurs and the time to short circuit (t_{sc}).[56,57] For the **C2400** separator, short circuits occurred rapidly (t_{sc} =30h, corresponding to 5 C cm^{-2}), consistent with prior studies by Tikekar et al..[58] This is attributed to highly heterogeneous current flow through the partially wetted separator, leading to localized high current densities and rapid growth of lithium dendrites.[59] In contrast, cells using functionalized separators **C6–C9** demonstrated significant performance enhancement, with no short circuits observed even after 1000 hours of cycling (~180 C cm^{-2}, **Figure 5a**). This represents

at least a 36-fold improvement in cycle life. Testing was stopped at 1000 hours, indicating the potential for even longer durability. The U-shaped voltage profiles of each half-cycle (**Figure 5b**) align with the mechanism proposed by Wood et al.,[60] wherein fresh lithium cycles at low potential, while increased potentials at the cycle's end reflect lithium use beneath the native solid electrolyte interphase (SEI) layer. Operando galvanostatic impedance measurements during cycling reveal that the high-frequency electrolyte resistances for functionalized separators remain stable over time (Nyquist diagrams, **Figure S24**). This stability reflects homogeneous lithium plating/stripping. At mid-frequencies, interfacial resistances decrease and stabilize for separators **C7**, **C8**, and **C9**, indicating the formation of a stable SEI. These observations confirm that functionalized separators significantly enhance the cycle life of Li/Li cells, likely due to more uniform current distribution at the Li/separator interface. Given their superior performance, separators **C6–C9** were further implemented in lithium batteries with two different configurations: Li/NMC and graphite/NMC.

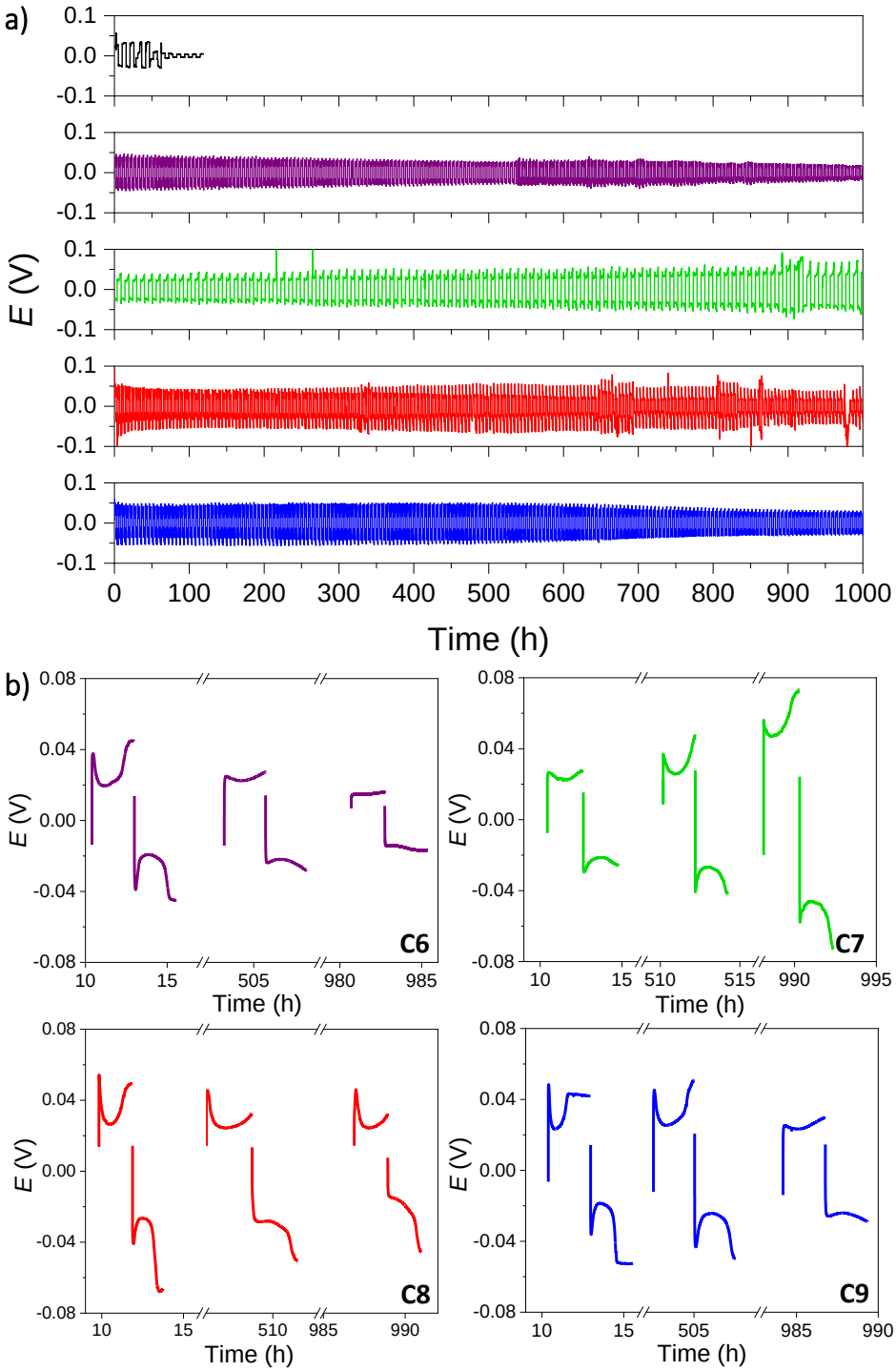

Figure 5. a) Galvanostatic cycling at ±50 µA cm^{-2} (4h long cycles) of symmetric Li/Li cells using the **C2400** separator (black) or functionalized separators **C6** (purple), **C7** (green), **C8** (red) and **C9** (blue). b) Magnification of selected cycles for functionalized separators **C6**–**C9**.

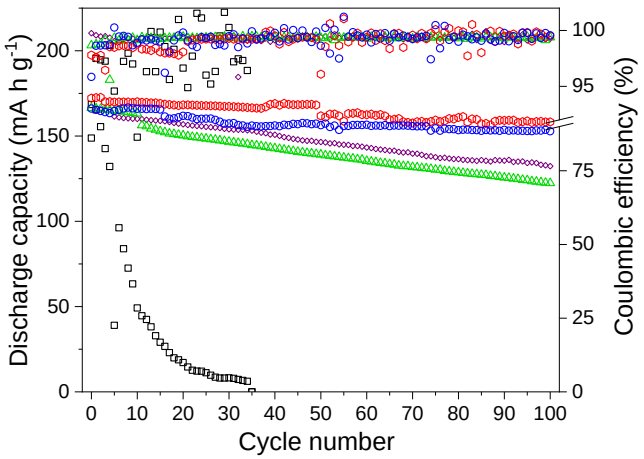

Figure 6. Discharge capacity and coulombic efficiency of Li/NMC622 batteries using a **C2400** separator (black squares) or functionalized separators **C6** (open purple diamonds), **C7** (open green triangles), **C8** (open red hexagons) and **C9** (open blue circles) for galvanostatic cycling with potential limitations at 4.2 V in charge and 3.0 V in discharge. The first ten cycles are obtained at C/10 and the next ninety cycles at C/5. Charge-discharge profiles for the third cycles are shown in **Figure S25**.

Electrochemical Characterization of Lithium Metal Batteries. To evaluate long-term cycling performance, the pristine **C2400** and functionalized separators were soaked with LP30 (60 µL) and assembled in coin cells with a NMC622-based positive electrode (2 mAh cm^{-2} areal capacity) and a 50 µm thick lithium foil as the negative electrode. Galvanostatic cycling was conducted over 100 cycles (10 cycles at *C*/10 followed by 90 cycles at *C*/5). The representative charge-discharge profiles for the third cycle of each cell (**Figure S25**) show the significant reduction of polarization for cells assembled with functionalized separators **C7–C9**. The battery using the **C2400** separator exhibited rapid capacity fade, with an initial discharge capacity of 154.0 mAh g^{-1} (**Figure 6**). The first short circuit, attributed to dendrite growth, occurred after only 5 cycles, consistent with Li/Li symmetric cell results. Conversely, batteries with functionalized separators **C6–C9** maintained

high discharge capacities throughout the cycling experiment. Two distinct behaviors were observed depending on the copolymer's chemical structure. Separators **C6** and **C7**, incorporating sulfonate anions, showed a linear decrease in capacity, retaining 74.6% and 73.6% of the initial discharge capacity (151.3 and 152.1 mAh g^{-1}, respectively) after 100 cycles. In contrast, separators **C8** and **C9**, containing TFSI anions, demonstrated higher capacity retention, with 91.8% and 92.0% of the initial discharge capacity (157.7 and 151.8 mAh g^{-1}, respectively) after 100 cycles. For all functionalized separators, coulombic efficiencies remained stable around 99.3% (**Figure 6**). The superior cycling performance of separators **C8** and **C9**, despite comparable wettability and lower Li-content compared to **C6** and **C7**, is attributed to the enhanced solvation of lithium sulfonimide ion pairs in carbonates, leading to improved electrochemical reversibility. Enhanced swelling of copolymers **8** and **9** (**Table S3**) also facilitates access to additional Li^+ ions within the pores, further supporting cycling stability. To assess power performance, coin cells were subjected to varying discharge rates (*D*/10 to 3*D*) at 25 °C, using a fast protocol (**Figure 7**).[61] At *D*/10, functionalized separators **C6–C9** exhibited similar discharge capacities (97.1–99.5% of initial capacity C_0), outperforming the **C2400** separator (93.8%). At higher discharge rates, the **C2400** separator showed drastic capacity fading, retaining only 11.0% of the initial capacity at 3*D*. Functionalized separators **C6–C9** significantly mitigated this issue, retaining 62.9–72.2% of the initial capacity at 3*D*, demonstrating a 6.3–7.2-fold improvement in high-rate discharge capacity compared to the **C2400** separator.

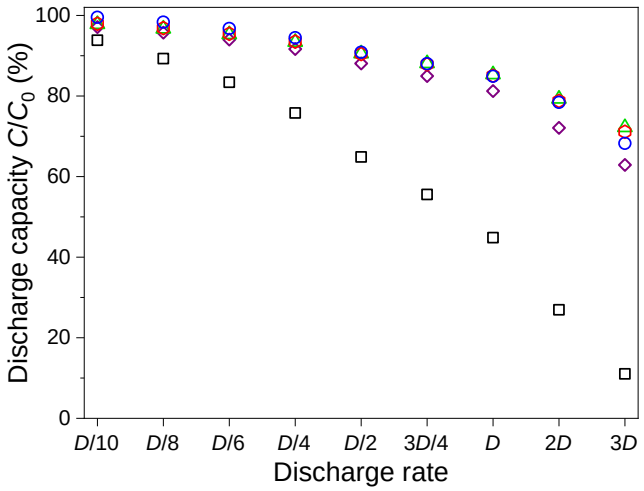

Figure 7. Power signature curves at 25 °C- Discharge capacities of **C2400** (open black squares) and functionalized separators **C6** (open purple diamonds), **C7** (open green triangles), **C8** (open red hexagons) and **C9** (open blue circles) as a function of the discharge rate.

Electrochemical Characterization of Lithium-Ion Batteries. LiBs were assembled using commercial composite electrodes (graphite negative and NMC622 positive; *N/P* = 1.2) and either the **C2400** or functionalized **C8** separator. To mimic industrial conditions, where electrolyte volume is minimized, the amount of LP30 was varied from 90 µL (12× the separator's porous volume) to 15 µL (2× the porous volume). Batteries were cycled at *C*/5 for charge and *D*/2 for discharge after a single formation cycle at *C*/10-*D*/10 (**Figure 8**). With the **C2400** separator, only the largest electrolyte excess (90 µL) provided adequate wetting and cycling performance, yielding a reversible capacity of 158.3 mAh g^{-1}. At reduced electrolyte volumes (60 µL or less), the **C2400** separator's performance deteriorated sharply, with reversible capacity dropping to 99.8 mAh g^{-1} at 60 µL. Below 30 µL of LP30, the battery failed to cycle due to insufficient ionic conductivity resulting from limited wetting. In contrast, LiBs with the **C8** separator cycled efficiently even at the lowest LP30 volume (15 µL), delivering stable and reversible performance. These results

underscore the advantages of functionalized separators in reducing process and material costs while maintaining excellent cycling and power performance.

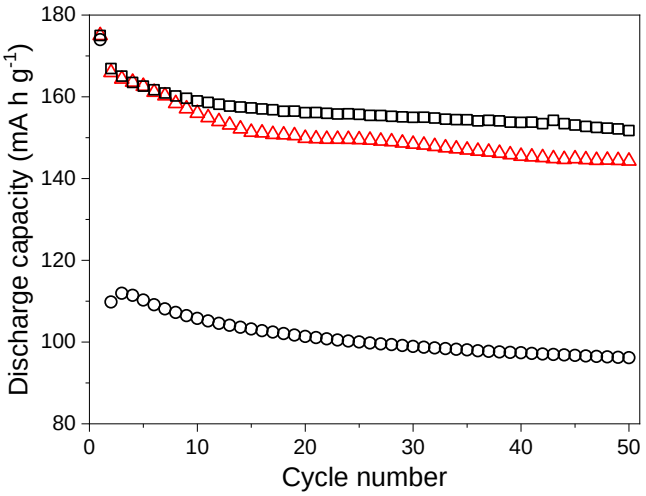

Figure 8. Discharge capacities obtained at 25 °C during galvanostatic cycling of graphite/NMC622 LiBs including a **C2400** separator + 90 µL (open black squares) or 60 µL (open black circles) of LP30, and a functionalized separator **C8** + 15 µL of LP30 (open red triangles) with potential limitations at 4.2 V *vs* Li in charge and 2.7 V *vs* Li in discharge. The rate is *C*/5 in charge and *D*/2 in discharge with a first formation cycle at *C*/10-*D*/10.

CONCLUSIONS

We have developed a versatile and scalable strategy to functionalize commercial polyolefin separators with photo-cross-linked single-ion statistical copolymer electrolytes (SIPEs). Utilizing less than 5 wt% of SIPEs, the method achieved strong anchoring within separator pores, ensuring stability in common solvents and preserving pore morphology with only minimal porosity reduction (~2%). The functionalized separators exhibited significantly enhanced wettability and

electrolyte uptake, resulting in effective ionic conductivities (σ_{eff}) that were 3–4 times higher than those of the pristine **C2400** separator. The superior performance of the **C8** and **C9** separators was attributed to the solvation of grafted TFSI-Li moieties by LP30, which provided additional Li^+ ions into the separator pores. In contrast, separators functionalized with sulfonate anions (**C6** and **C7**) demonstrated lower σ_{eff}, primarily due to less effective solvation and non-uniform coatings, as revealed by SEM analysis. Cycling tests in Li/Li symmetric cells further highlighted the advantages of functionalized separators, particularly their ability to sustain highly reversible lithium plating and stripping for over 1000 hours at ±50 μA cm^{-2}, without short-circuiting. The untreated **C2400** separator, by comparison, failed after 30 hours due to poor wettability and localized current density variations. In full-cell configurations, the functionalized separators significantly improved cycling stability and power performance (7-fold increase at 3*D*-rate). Long-term tests confirmed sustained discharge capacities over 100 cycles, reduced polarization, and more uniform utilization of active materials. Notably, the **C8** and **C9** separators outperformed **C6** and **C7** in capacity retention, despite comparable wettability, due to the superior solvation properties of lithium sulfonimide ion pairs and their enhanced swelling behavior, which increased accessibility to Li^+ ions. Furthermore, these separators enabled efficient operation with reduced electrolyte volumes, underscoring their potential for industrial applications. This work introduces a straightforward and tunable approach for designing high-performance separators for lithium-ion and lithium-metal batteries. The method's flexibility allows for macromolecular design customization to meet the specific requirements of diverse liquid-based battery systems. For instance, while this work has shown that both positive and negative electrodes work more homogeneously, limiting the current density dispersion, improving the cycle life-mitigation of shorts due to lithium dendrites, which corresponds *de facto* to an improvement of the safety of the

battery under operation, extension to other monomers such as phosphate-based monomers known for the anti-flammability properties of the corresponding polymers would contribute to improve safety. Finally, this surface functionalization strategy could be advantageously applied to other types of commercial porous separators allowing safety improvements, e.g. alumina-coated polyolefin porous separators. By improving cycle life, power output, and assembly efficiency, the functional separators developed herein represent a pivotal advancement in next-generation battery technologies. This work paves the way for safer, more efficient, and cost-effective batteries, broadening the scope of applications for liquid-based energy storage systems.

ASSOCIATED CONTENT

Supporting Information

The Supporting Information is available free of charge on the ACS Publications website at DOI: 10.1021/acsami.xxxxxxx.

Experimental details, synthesis, structure, composition, solubility, NMR, DSC and TGA traces for copolymers **6–9**. Electrolyte uptakes, contact angles, SEM, SEM/EDX and N_2 adsorption/desorption isotherms for **C2400** separator and functionalized separators **C6–C9**. Schematic representation of the cells used for electrochemical measurements, photo-cross-linking kinetics and electrochemical impedance spectroscopy on Li/Li cells. (PDF) Video showing the wet coating deposition process. (MP4)

AUTHOR INFORMATION

Corresponding Authors

Renaud Bouchet – Univ. Grenoble Alpes, Univ. Savoie Mont Blanc, CNRS, Grenoble INP, LEPMI, 38000 Grenoble, France; orcid.org/0000-0002-4040-2253; Email: renaud.bouchet@grenoble-inp.fr

Eric Drockenmuller –Université Claude Bernard Lyon 1, CNRS, Ingénierie des Matériaux Polymères, UMR 5223, F-69622 Villeurbanne, France; orcid.org/0000-0003-0575-279X; Email: eric.drockenmuller@univ-lyon.fr

Authors

Valentin Vinci – Université Grenoble Alpes, Université Savoie Mont Blanc, CNRS, Grenoble INP, LEPMI, 38000 Grenoble, France; orcid.org/0009-0008-2412-2842

Dimitri Flachard – Université Claude Bernard Lyon 1, CNRS, Ingénierie des Matériaux Polymères, UMR 5223, F-69622 Villeurbanne, France; orcid.org/0000-0001-7250-1072

Helena Henkel – Université Claude Bernard Lyon 1, CNRS, Ingénierie des Matériaux Polymères, UMR 5223, F-69622 Villeurbanne, France; orcid.org/0000-0002-2068-1910

Author Contributions

The manuscript was written through contributions of all authors. All authors have given approval to the final version of the manuscript.

Notes

The authors declare no competing financial interest.

ACKNOWLEDGMENTS

Authors gratefully acknowledge the financial support from the “Région Rhône-Alpes Auvergne”, the SATT Pulsalys, and the European Union through HORIZON EUROPE Marie Sklodowska-Curie Actions - RIDERS Doctoral Network (grant agreement nr. 101120432).

REFERENCES

(1) Tarascon, J.-M.; Armand, M. Issues and Challenges Facing Rechargeable Lithium Batteries. *Nature* **2001**, 414, 359–367.

(2) Deng, D. Li-Ion Batteries: Basics, Progress, and Challenges. *Energy Sci. Eng.* **2015**, 3(5), 385–418.

(3) Li, M.; Lu, J.; Chen, Z.; Amine, K. 30 Years of Lithium-Ion Batteries. *Adv. Mater.* **2018**, 30, 1800561.

(4) Duan, J.; Tang, X.; Dai, H.; Yang, Y.; Wu, W.; Wei, X.; Huang, Y. Buildig Safe Lithium-Ion Batteries for Electric Vehicles; A Review. *Electrochem. Energy Rev.* **2020**, 3, 1–42.

(5) Yang, Z.; Zhang, J.; Kintner-Meyer, M. C. W.; Lu, X.; Choi, D.; Lemmon, J. P.; Liu, J. Electrochemical Energy Storage for Green Grid. *Chem. Rev.* **2011**, 111, 3577–3613.

(6) Cavers, H.; Molaiyan, P.; Abdollahifar, M.; Lassi, U.; Kwade, A. Perspectives on Improving the Safety and Sustainability of High Voltage Lithium-Ion Batteries Through the Electrolyte and Separator Region. *Adv. Energy Mater.* **2022**, 12, 2200147.

(7) Larcher, D.; Tarascon, J.-M. Towards greener and more sustainable batteries for electrical storage. *Nature Chem.* **2015**, 7, 19–29.

(8) Tang, Y.; Zhang, Y.; Li, W.; Ma, B.; Chen, X. Rational material design for ultrafast rechargeable lithium-ion batteries. *Chem. Soc. Rev.* **2015**, 44, 5926–5940.

(9) Blomgren, G.E. The development and Future of Lithium Ion Batteries. *J. Electrochem. Soc.* **2017**, *164*, 5019–5025.

(10) Xu, K. Electrolytes and Interphases in Li-Ion Batteries and Beyond. *Chem. Rev.* **2014**, 114, 11503–11618.

(11) Arora, P.; Zhang, Z. J. Battery Separators. *Chem. Rev.* **2004**, 104, 4419−4462.

(12) Deimede, V.; Elmasides, C. Separators for Lithium-Ion Batteries: A Review on the Production Processes and Recent Developments. *Energy Technol.* **2015**, 3, 453–468.

(13) Lu, W.; Yuan, Z.; Zhao, Y.; Zhang, H.; Zhang, H.; Li, X. Porous Membranes in Secondary Battery Technologies. *Chem. Soc. Rev.* **2017**, 46, 2199–2236.

(14) Lagadec, M.F.; Zahn, R; Wood, V. Characterization and performance evaluation of lithium-ion battery separators. *Nat. Energy* **2019**, 4, 16–19.

(15) Luiso, S.; Fedkiw, P. Li-ion battery separators: recent developments and state-of-art. *Curr. Opin. Electrochem.* **2020**, 20, 99–107.

(16) Huang, X. Z.; He, R.; Li, M.; Chee, M. O. L.; Dong, P.; Lu, J. Functionalized separator for next-generation batteries. *Mater. Today* **2020**, 41, 143–155.

(17) Zahn, R.; Lagadec, M. F.; Hess, M.; Wood, V. Improving Ionic Conductivity and Lithium-Ion Transference Number in Lithium-Ion Battery Separators. *ACS Appl. Mater. Interfaces* **2016**, 8, 32637−32642.

(18) Zhai, P.; Liu, K.; Wang, Z.; Shi, L.; Yuan, S. Multifunctional separators for high-performance lithium ion batteries. *J. Power Sources* **2021**, 499, 229973.

(19) Badiker, D. M. D.; Usha, Z. R.; Wan, C.; Hassaan, M. M. E.; Chen, X.; Li, L. Recent progress of composite polyethylene separators for lithium/sodium batteries. *J. Power Sources* **2023**, 564, 232853.

(20) Deng, Z.; Huang, Z. Y.; Shen, Y.; Huang, Y.H.; Ding, H.; Luscombe, A.; Johnson, M.; Harlow, J. E.; Gauthier, R.; Dahn, J.R. Ultrasonic Scanning to Observe Wetting and Unwetting in Li-Ion Pouch Cells. *Joule* **2020**, 4, 2017–2029.

(21) Djian, D.; Alloin, F.; Martinet, S.; Lignier, H.; Sanchez, J. Y. Lithium-Ion Batteries with High Charge Rate Capacity: Influence of the Porous Separator. *J. Power Sources* **2007**, 172, 416–421.

(22) Thorat, I. V.; Stephenson, D. E.; Zacharias, N. A.; Zaghib, K.; Harb, J. N.; Wheeler, D. R. Quantifying Tortuosity in Porous Li-Ion Battery Materials. *J. Power Sources* **2009**, 188, 592–600.

(23) Devaux, D.; Chang, Y. H.; Villaluenga, I.; Chen, X. C.; Chintapalli, M.; DeSimone, J. M.; Balsara, N. P. Conductivity of Carbonate- and Perfluoropolyether-Based Electrolytes in Porous Separators. *J. Power Sources* **2016**, 323, 158–165.

(24) Zheng, J., Lochala, J. A., Kwok, A., Deng, Z. D.; Xiao, J. Research Progress toward Understanding the Unique Interfaces between Concentrated Electrolytes and Electrodes for Energy Storage Applications. *Adv. Sci.* **2017**, 170032;

(25) Ko, J. M.; Min, B. G.; Kim, D.-W.; Ryu, K. S.; Kim, K. M.; Chang, S. H. Thin-film type Li-ion battery, using a polyethylene separator grafted with glycidyl methacrylate. *Electrochim. Acta* **2004**, 50, 367–370.

(26) Gao, K.; Hu, X.; Yi, T.; Dai, C. PE-g-MMA Polymer Electrolyte Membrane for Lithium Polymer Battery. *Electrochim. Acta* **2006**, 52, 443–449.

(27) Gwon, S.-J.; Choi, J.-H.; Sohn, J.-Y.; Ihm, Y.-E.; Nho, Y.-C. Preparation of a New Micro-porous Poly(methyl methacrylate)-grafted Polyethylene Separator for High Performance Li Secondary Battery. *Nucl. Instr. Meth. Phys. Res. B* **2009**, 267, 3309–3313.

(28) Lee, J. Y.; Bhattacharya, B.; Nho, Y. C.; Park, J.-K. New Separator Prepared by Electron Beam Irradiation for High Voltage Lithium Secondary Batteries. *Nucl. Instr. Meth. Phys. Res. B* **2009**, 267, 2390–2394.

(29) Ryou, M.-H.; Lee, Y.M.; Park, J.-K.; Choi ,J. Mussel-Inspired Polydopamine-Treated Polyethylene Separators for High-Power Li-Ion Batteries. W. *Adv. Mater.* **2011**, 23, 3066–3070.

(30) Lee, Y.; Ryou, M.-H.; Seo, M.; Choi, J. W.; Lee, Y. M. Effect of Polydopamine Surface Coating on Polyethylene Separators as a Function of their Porosity for High-Power Li-Ion Batteries. *Electrochim. Acta* **2011**, 113, 433– 438.

(31) Pan, L.; Wang, H.; Wu, C.; Liao, C.; Li, L. Tannic acid coated polypropylene membrane as separator for lithium-ion batteries. *ACS Appl. Mater. Interfaces* **2015**, 729, 16003-16010.

(32) Chen, W.; Shi, L.; Wang, Z.; Zhu, J.; Yang, H.; Mao, X.; Chi, M.; Sun, L.; Yuan, S. Porous Cellulose Diacetate-SiO_2 Composite Coating on Polyethylene Separator for High-Performance Lithium-Ion Battery. *Carbohyd. Polym.* **2016**, 147, 517–524.

(33) Fang, L.-F.; Shi, J.-L.; Zhu, B.-K.; Zhu, L.-P. Facile Introduction of Polyether Chains onto Polypropylene Separators and its Application in Lithium Ion Batteries. *J. Membrane Sci.* **2013**, 448, 143–150.

(34) Liao, H.; Zhang., H.; Hong, H.; Li, Z.; Qin, G.; Zhu, H.; Lin, Y. Novel Cellulose Aerogel Coated on Polypropylene Separators as Gel Polymer Electrolyte with High Ionic Conductivity for Lithium-Ion Batteries. *J. of Membrane Sci.* **2016**, 514, 332–339.

(35) Hu, S.; Lin, S.; Tu, Y.; Hu, J.; Wu, Y.; Liu, G.; Li, F.; Yu, F.; Jiang, T. Novel Aramid Nanofiber-Coated Polypropylene Separators for Lithium Ion Batteries. *J. Mater. Chem. A* **2016**, 4, 3513–3526.

(36) Shi, J.-L.; Fang, L.-F.; Li, H.; Zhang, H.; Zhu, B.-K.; Zhu, L.-P. Improved Thermal and Electrochemical Performances of PMMA Modified PE Separator Skeleton Prepared via Dopamine-initiated ATRP for Lithium Ion Batteries. *J. Memb. Sci.* **2013**, 437, 160–168.

(37) Rao, E.; McVerry, B.; Borenstein, A.; Anderson, M.; Jordan, R. S.; Kaner, R. B. Roll-to-Roll Functionalization of Polyolefin Separators for High- Performance Lithium-Ion Batteries. *ACS Appl. Energy Mater.* **2018**, 1, 3292−3300.

(38) Stokes, K. K.; Humitson, K. F. Surface Modified Polymeric Materials, Modified Functionalized Polymers, Functional Polymers and Methods. US 20180358594 A1, December 13, 2018.

(39) Al Akhrass, S.; Gal, F.; Damiron, D.; Alcouffe, P.; Hawker, C. J.; Cousin, F.; Carrot, G.; Drockenmuller, E. Design of Crosslinked Hybrid Multilayer Thin Films from Azido-Functionalized Polystyrenes and Platinum Nanoparticles. *Soft Matter* **2009**, 5, 586–592.

(40) Schuh, K.; Prucker, O.; Rühe, J. Tailor-Made Polymer Multilayers. *Adv. Funct. Mater.* **2013**, 23 (48), 6019–6023.

(41) Pandiyarajan, C. K.; Genzer, J. Thermally Activated One-Pot, Simultaneous Radical and Condensation Reactions Generate Surface-Anchored Network Layers from Common Polymers. *Macromolecules* **2019**, 52 (2), 700–707.

(42) Kim, D.-W.; Ko, J.-M.; Chun, J.-H.; Kim, S.-H.; Park, J.-K. Electrochemical Performances of Lithium-Ion Cells Prepared with Polyethylene Oxide-coated Separators. *Electrochem. Commun.* **2001**, 3, 535–538.

(43) Sohn, J.-Y.; Im, J.-S.; Shin, J.; Nho, Y.-C. PVDF-HFP/PMMA-coated PE Separator for Lithium Ion Battery. *J. Solid. State Electr.* **2012**, 16 (2), 551–556.

(44) Song, J.; Ryou, M.-H.; Son, B.; Lee, J.-N.; Lee, D. J.; Lee, Y. M.; Choi, J. W.; Park, J.-K. Co-polyimide-coated Polyethylene Separators for Enhanced Thermal Stability of Lithium Ion Batteries. *Electrochim. Acta* **2012**, 85, 524–530.

(45) Landesfeind, J.; Hattendorff, J.; Ehrl, A.; Wall, W. A.; Gasteiger, H. A. Tortuosity Determination of Battery Electrodes and Separators by Impedance Spectroscopy. *J. Electrochem. Soc.* **2016**, *163* (7), 1373–1387.

(46) Jaeger, W.; Bohrisch, J.; Laschewsky, A. Synthetic polymers with quaternary nitrogen atoms Synthesis and structure of the most used type of cationic polyelectrolytes. *Prog. Polym. Sci.* **2010**, 35, 511–577.

(47) Shaplov, A. S.; Ponkratov, D. O.; Vygodskii, Y. S. Poly(ionic liquid)s: Synthesis, Properties, and Application. *Polym. Sci. Ser. B* **2016**, 58(2), 73–142.

(48) Szabo, A; Wacha, A; Thomann, R; Szarka, G; Bota, A; Ivan, B. Synthesis of Poly(methyl methacrylate)-poly(poly(ethylene glycol) methacrylate)-polyisobutylene ABCBA Pentablock Copolymers by Combining Quasiliving Carbocationic and Atom Transfer Radical Polymerizations and Characterization Thereof. *J. Macromol. Sci. A* **2015**, 52, 252–259.

(49) Albuszis, M.; Roth, P. J.; Pauer, W.; Moritz, H.-U. Two in one: Use of Azide Functionality for Controlled Photo-crosslinking and Click-modification of Polymer Microspheres. *Polym. Chem.* **2016**, 7, 5414–5425.

(50) Meziane, R.; Bonnet, J.-P.; Courty, M.; Djellab, K.; Armand, M. Single-ion Polymer Electrolytes Based on a Delocalized Polyanion for Lithium Batteries. *Electrochim. Acta* **2011**, 57, 14–19.

(51) Porcarelli, L.; Aboudzadeh, M. A.; Rubatat, L.; Nair, J. R.; Shaplov, A. S.; Gerbaldi, C.; Mecerreyes, D. Single-ion Triblock Copolymer Electrolytes Based on Poly(ethylene oxide) and

Methacrylic Sulfonamide Blocks for Lithium Metal Batteries. *J. Power Sources* **2017**, 364, 191–199.

(52) Kung, C. H.; Sow, P. K.; Zahiri, B.; Merida, W. Assessment and Interpretation of Surface Wettability Based on Sessile Droplet Contact Angle Measurement: Challenges and Opportunities. *Adv. Mater. Interfaces* **2019**, 1900839.

(53) Song, J. Y.; Wang, Y. Y.; Wan, C. C. Conductivity Study of Porous Plasticized Polymer Electrolytes Based on Poly(vinylidene fluoride) A Comparison with Polypropylene Separators. *J. Electrochem. Soc.* **2000**, 147, 3219.

(54) Bruggeman, D. A. G. Berechnung Verschiedener Physikalischer Konstanten von Heterogenen Substanzen. *Ann. Phys.* **1935**, 24, 636–664.

(55) Rosso, M.; Gobron, T. Brissot, C.; Chazalviel, J.-N.; Lascaud, S. Onset of Dendritic Growth in Lithium/Polymer Cells. *J. Power Sources* **2001**, 97–98, 804–806.

(56) Sannier, L.; Bouchet, R.; Rosso, M.; Tarascon, J.-M. Evaluation of GP56 E performances in lithium metal battery technology by means of simple polarization tests. *J. Power Sources* **2006**, 158, 564-570.

(57) Brissot, C.; Rosso, M.; Chazalviel, J. -N.; Lascaud, S. In Situ Concentration Cartography in the Neighborhood of Dendrites Growing in Lithium/Polymer-Electrolyte/Lithium Cells. *J. Electrochem. Soc.* **1999,** 146(12), 4393–4400.

(58) Tikekar, M. D.; Archer, L. A.; Koch, D. L. Stability Analysis of Electrodeposition Across a Structured Electrolyte with Immobilized Anions. *J. Electrochem. Soc.* **2014**, 161, A847–A855.

(59) Rosso, M.; Brissot, C.; Teyssot, A.; Dollé, M.; Sannier, L.; Tarascon, J.-M.; Bouchet, R.; Lascaud, S. Dendrite Short-circuit and Fuse Effect on Li/Polymer/Li cells. *Electrochim. Acta* **2006**, 51, 5334–5340.

(60) Wood, K. N.; Kazyak, E.; Chadwick, A. F.; Chen, K.-H.; Zhang, J-.G.; Thornton, K.; Dasgupta, N. P. Dendrites and Pits: Untangling the Complex Behavior of Lithium Metal Anodes through Operando Video Microscopy. *ACS Cent. Sci.* **2016**, 2 11, 790–801.

(61) Devaux, D.; Leduc, H.; Dumaz, P.; Lecuyer, M.; Deschamps, M.; Bouchet, R. Effect of Electrode and Electrolyte Thicknesses on All-Solid-State Battery Performance Analyzed With the Sand Equation. *Front. Energy Res.* **2020**, 7, 168.

GRAPHICAL ABSTRACT

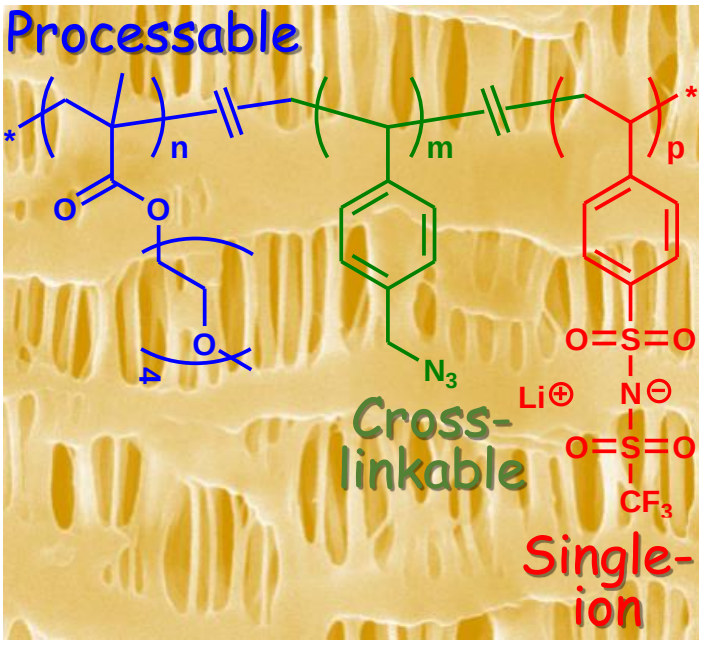

Supporting Information

Enhancing Performances of Lithium Batteries through Functionalization of Porous Polyolefin Separators with Cross-linked Single-Ion Polymer Electrolytes

Valentin Vinci,[1] Dimitri Flachard,[1,2] Helena Henke,[2] Renaud Bouchet,[1,] and Eric Drockenmuller,[2,*]*

[1] Université Grenoble Alpes, Univ. Savoie Mont Blanc, CNRS, Grenoble INP, LEPMI, 38000 Grenoble, France

[2] Université Claude Bernard Lyon 1, CNRS, Ingénierie des Matériaux Polymères, UMR 5223, Villeurbanne, F-69622, France

[*] Renaud Bouchet, Email: renaud.bouchet@grenoble-inp.fr.

[*] Eric Drockenmuller, Email: eric.drockenmuller@univ-lyon.fr.

Table S1. Representative literature data on the physical properties of chemically modified porous polyolefin separators for lithium-ion batteries.

Ref.	Separator	Process[a]	Deposited material	Liquid electrolyte	Contact angle untreated (functionalized)[b]	*EU* (%) untreated (functionalized)[b]	σ' (mS cm^{-1}) untreated (functionalized)	Improvement factor (*F*)[c]
26	PE Asahi Kasei 25 µm	EBI	Poly(methyl methacrylate)	1M $LiPF_6$ EC/DMC (1:1 v/v)	/ /	115 (210)	0.05 (1.01)	20.2
27	PE Asahi Kasei 20µm	γRI	Poly(methyl methacrylate)	1M $LiClO_4$ EC/PC (1:1 v/v)	/ /	30 (320)	0.095 (1.4)	14.7
28	PE 20 µm	EBI	Poly[poly(ethylene glycol) borate acrylate]	1M $LiPF_6$ EC/DMC (1:1 v/v)	/ /	/ /	0.49 (0.62)	1.3
29	PE	RC	Polydopamine	1M $LiPF_6$ EC/DEC/PC (3:6.5:0.5 wt/wt/wt)	(H_2O) 108 (39)	96 (126)	0.23 (0.41)	1.8
30	PE 16 µm	RC	Polydopamine	1M $LiPF_6$ EC/DEC (1:2 v/v)	(H_2O)120 (46)	176 (202)	0.60 (0.87)	1.5
31	PP – Celgard 2400	RC	Tannic acid	1M $LiPF_6$ EC/DMC (1:1 wt/wt)	(H_2O) 120 (72)	90 (125)	0.23 (0.46)	2.0
32	PE 14 µm	RC	Cellulose diacetate/SiO_2 composite	1M $LiPF_6$ EC/DEC/EMC (1:1:1 wt/wt/wt)	/ /	110 (277)	0.397 (0.624)	1.6
33	PP – Celgard 2500	GT	Poly(ethylene glycol)	1M $LiPF_6$ EC/EMC/DMC (1:1:1 wt/wt/wt)	45 (15)	96 (122)	0.95 (0.99)	1.0
34	PP – Celgard 2400 25µm	GT	Hydroxyethylcellulose	1M $LiPF_6$ EC/DEC/DMC (1:1:1 wt/wt/wt)	/ /	180 (800)	0.95 (2.03)	2.1
35	PP 20 µm	GT	Aramid nanofibers	1M $LiPF_6$ DMC/EC/PC (2:1:1 wt/wt/wt)	(H_2O) 118 (133)	(H_2O) 95 (132)	0.56 (0.69)	1.2
36	PE	GF	Poly(methyl methacrylate)	1M $LiPF_6$ EC/DMC/DEC (1:1:1 wt/wt/wt)	36 (20)	116 (183)	1.15 (1.19)	1.2
37	PE/PP/PE – Celgard 2320	GT	Perfluorophenyl azide sulfobetaine	1M $LiPF_6$ EC/DMC (1:1 v/v)	(H_2O) 104 (54)	111 (314)	0.2 (0.47)	2.4
42	PE Asahi Kasei 25 µm	PA	Poly(ethylene glycol)	1M $LiBF_4$ EC/DMC (1:1 v/v)	/ /	/ /	0.18 (1.0)	5.6
43	PE 12 µm	PA	PVDFHFP/poly(methyl methacrylate) blends	1M $LiClO_4$ EC/DEC (1:1 v/v)	/ /	315 (403)	0.73 (1.7)	2.3
44	PE Asahi Kasei 20 µm	PA	Polyimide	1M $LiPF_6$ EC/DEC (1:1 v/v)	/ /	109 (106)	0.25 (0.24)	1.0

[a]: EBI = electron beam irradiation; γRI = γ-rays irradiation; RC = reactive coating; GT = grafting–to; GF = grafting–from; PA = physical adsorption.

[b]: Contact angle and electrolyte uptake for the electrolyte or H_2O when mentioned. [c]: Calculated by the ratio between the functionalized separator soaked by liquid electrolyte and the untreated separator.

Scheme S1. Structure of symmetric stainless-steel (SS) cells (**A**), symmetric lithium foil cells (**B**), Li/NMC batteries (**C**) and graphite/NMC batteries (**D**) wetted by a 1M $LiPF_6$ solution in a 1:1 (vol/vol) EC/DMC mixture (i.e. LP30) used for electrochemical impedance spectroscopy measurements performed using untreated **C2400** separator or functionalized separators **C6**–**C9**.

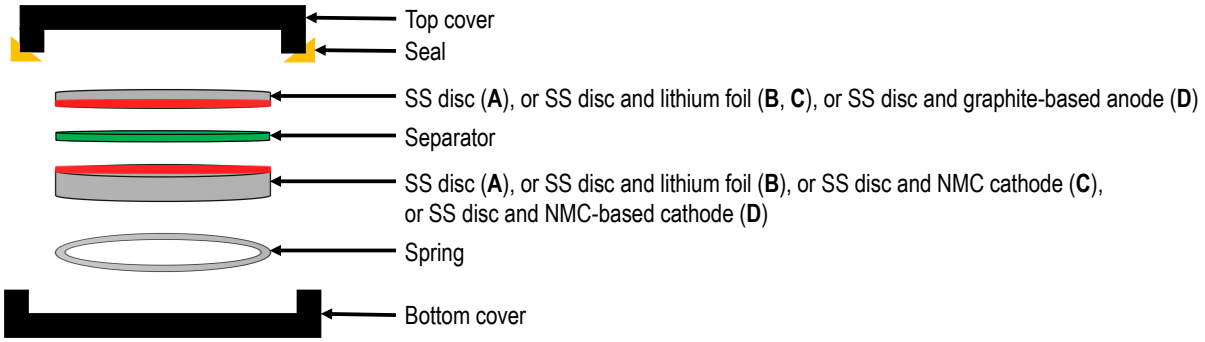

Scheme S2. Synthesis of lithium-containing single-ion statistical copolymer electrolytes by free radical solution copolymerization.

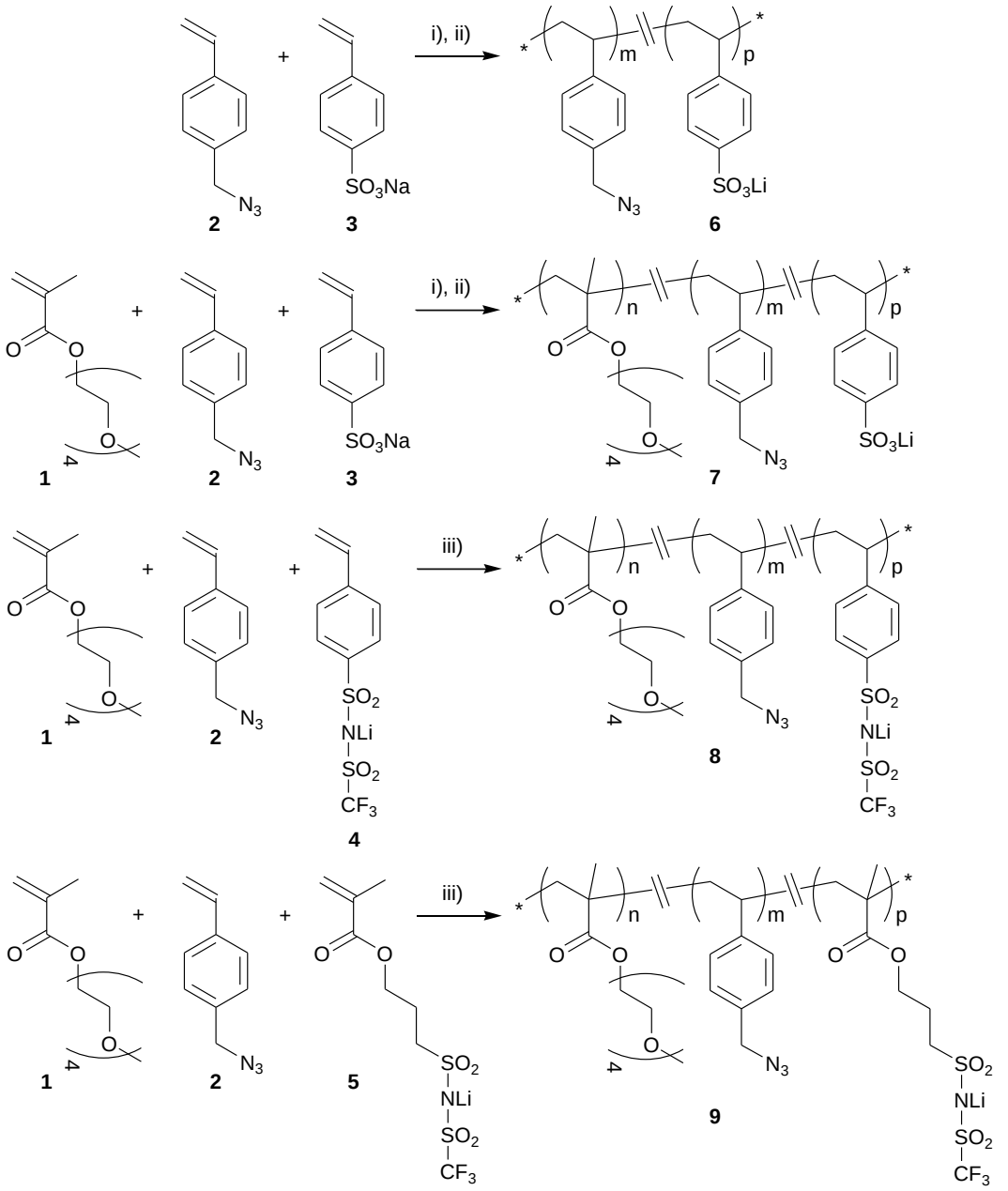

i) AIBN, H_2O/CH_3CN, 60 °C; ii) $LiClO_4$, H_2O, RT; iii) AIBN, DMF, 60 °C

Scheme S3. Chemical pathways leading to SIPE cross-linking and tethering to the polypropylene separator after UV irradiation of azide functionality.

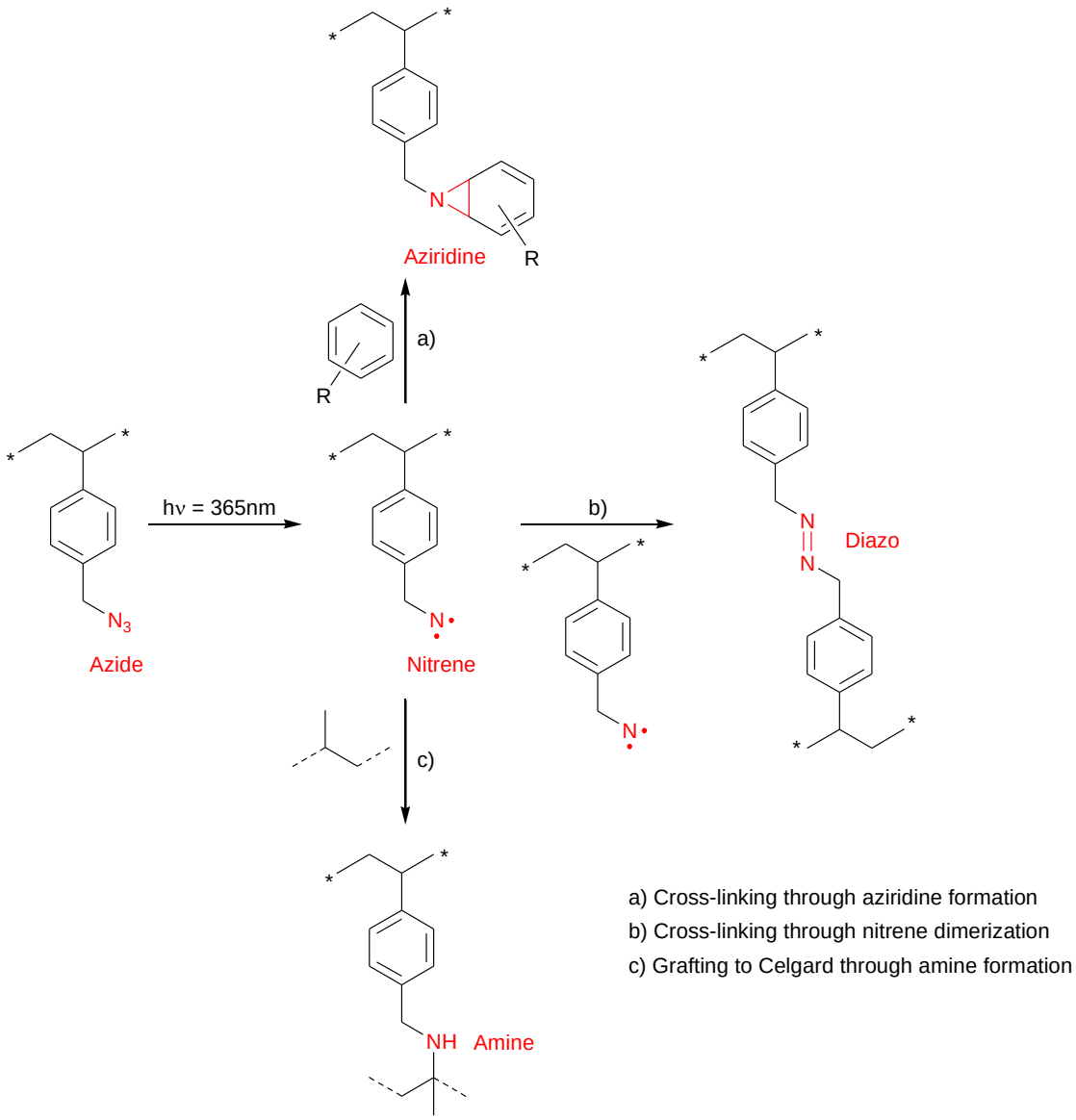

Table S2. Composition and thermal properties of copolymers **6**–**9**.

N°	n[a]	m[a]	p[a]	T_g (°C)[b]	T_{d10} (°C)[c]	M_n (kg mol^{-1})[d]	$Đ$[d]
6	/	0.10	0.90	/	390	/	/
7	0.22	0.14	0.64	/	350	120	4.9
8	0.30	0.15	0.55	65	295	172	2.2
9	0.33	0.19	0.48	43	260	183	3.1

[a]: Experimental molar ratios of monomer units in the copolymers determined by ^{1}H NMR. [b]: Determined by DSC. [c]: Determined by TGA. [d] Determined by SEC in DMSO at 65 °C.

Table S3. Solubility of lithium-containing single-ion statistical copolymers **6–9**.

	H_2O[a]	nC_7H_{16}	MeOH	EtOAc	Acetone	Et_2O	THF	CH_2Cl_2	$CHCl_3$	CH_3CN	$PhCH_3$	DMF	DMSO	EC/DMC
6	++	–	–	–	–	–	–	–	–	–	–	++	–	–
7	++	–	++	–	–	–	–	–	–	–	–	++	++	–
8	++	–	++	–	++	–	++	–	–	++	–	++	++	++
9	++	–	++	–	++	–	++	–	–	++	–	++	++	++

a] "++" indicates solubility at 10 mg mL^{-1}, "+" indicates solubility at 1 mg mL^{-1}, while "–" indicates no detectable solubility at 1 mg mL^{-1}.

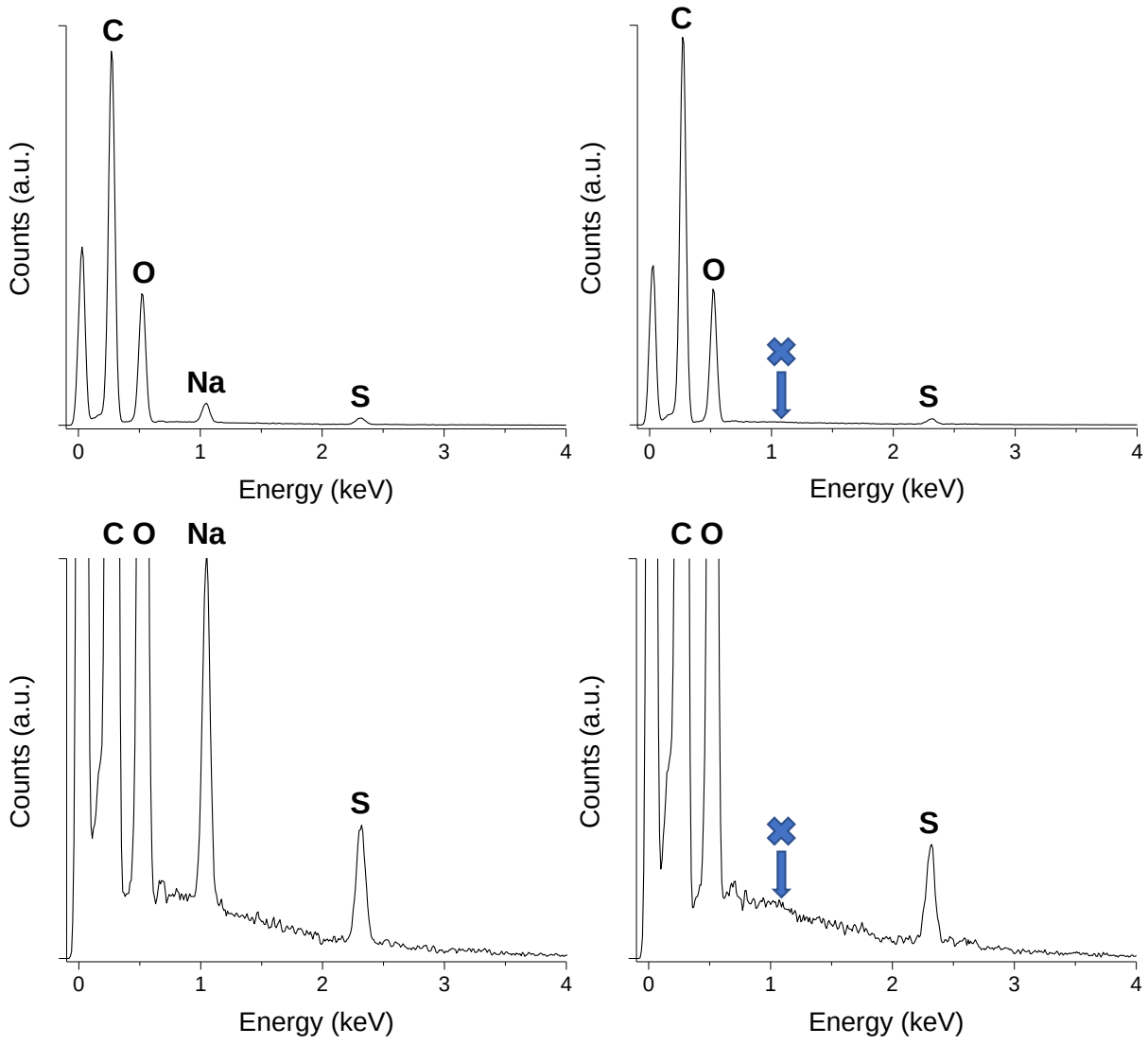

Figure S1. SEM/EDX microanalysis for dense membranes of copolymer **6** before (left graphs) and after (right graphs) ion exchange reaction to substitute sodium for lithium counter–cations.

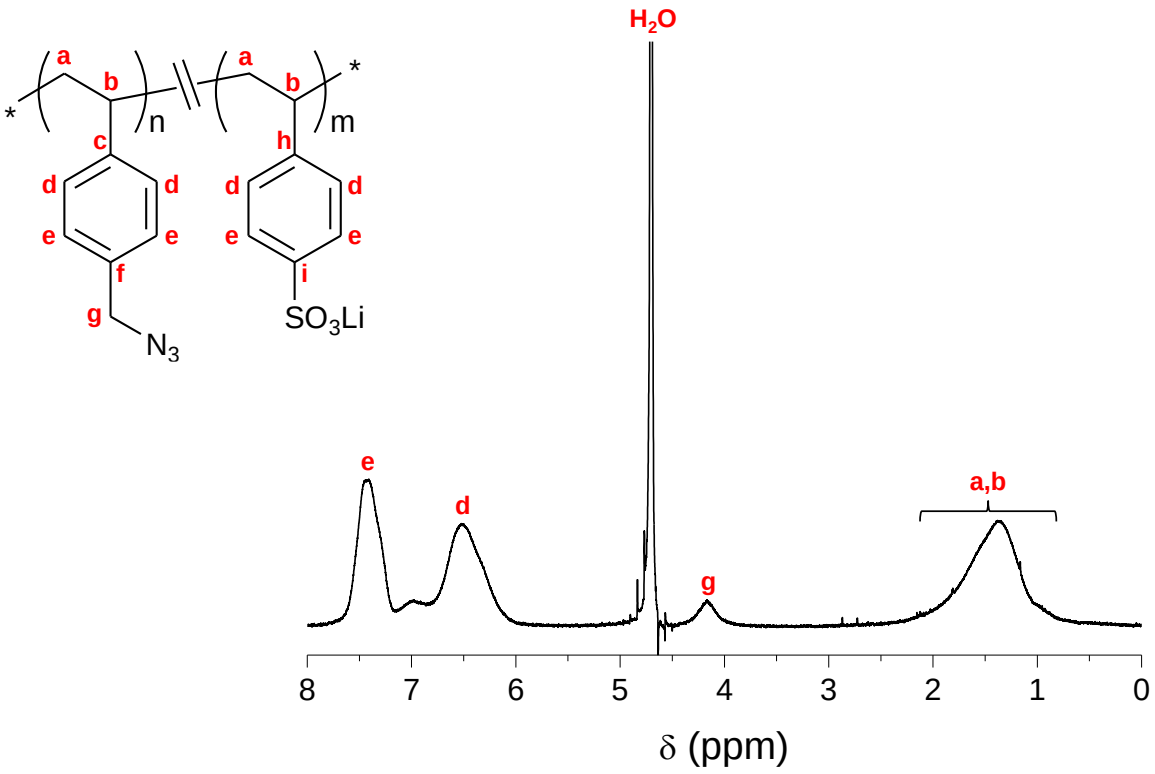

Figure S2. ^{1}H NMR of lithium–containing single–ion copolymer electrolyte **6** in D_2O.

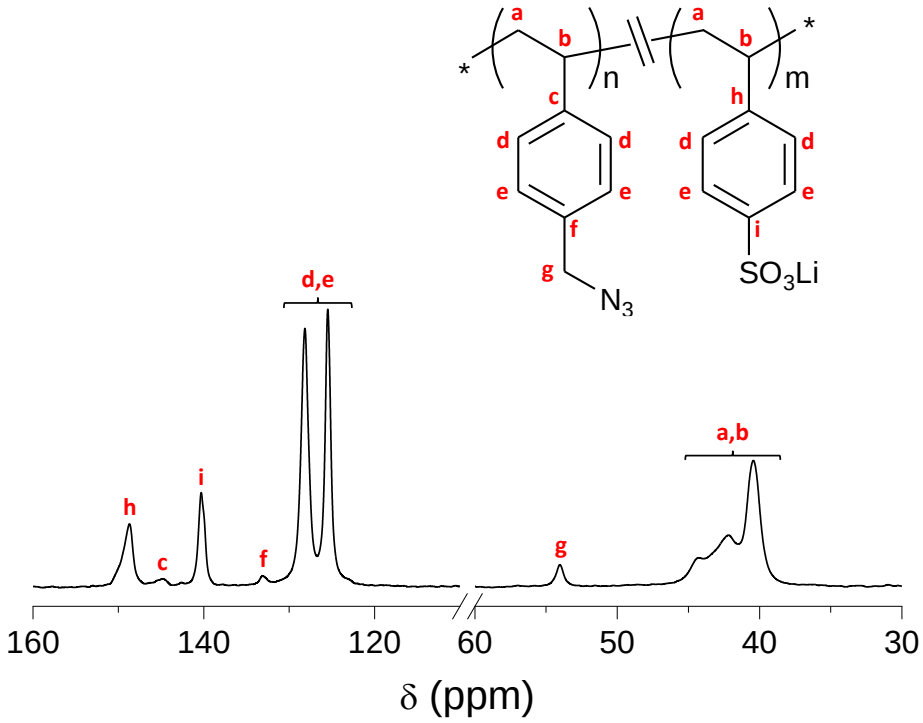

Figure S3. ^{13}C NMR of lithium–containing single–ion copolymer electrolyte **6** in D_2O.

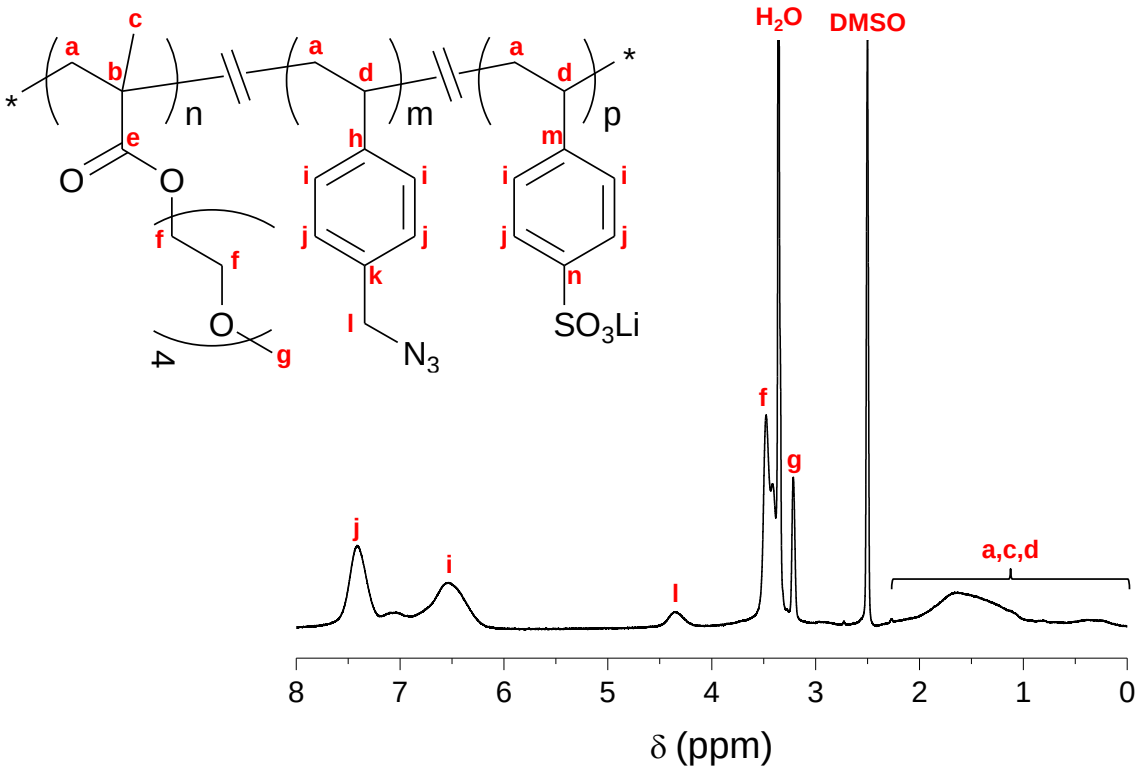

Figure S4. ^{1}H NMR of lithium–containing single–ion copolymer electrolyte **7** in DMSO–d_6.

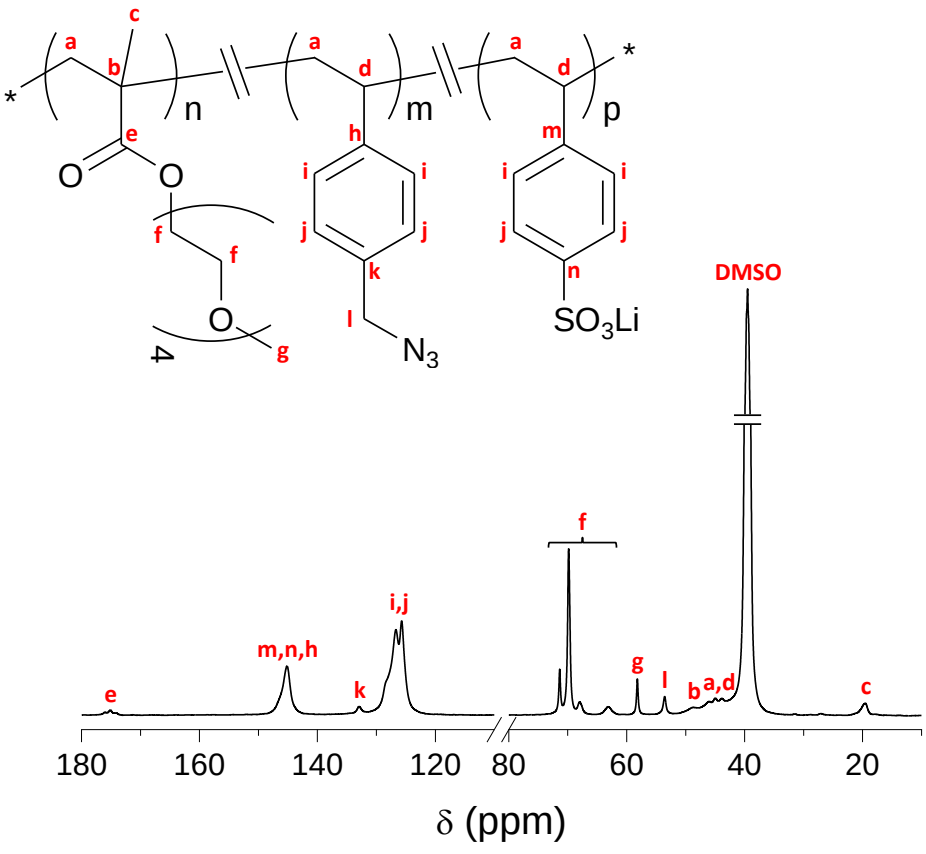

Figure S5. ^{13}C NMR of lithium–containing single–ion copolymer electrolyte **7** in DMSO–d_6.

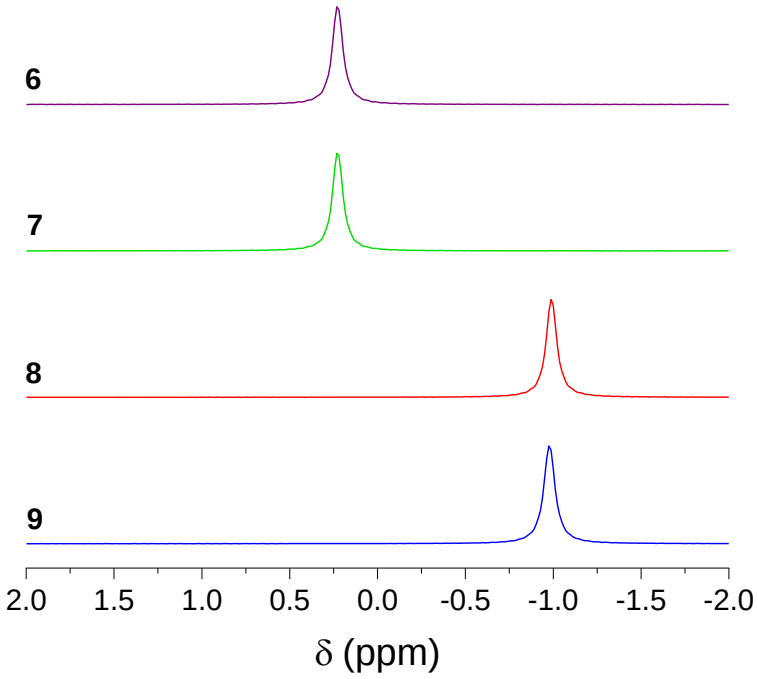

Figure S6. ^{7}Li NMR of lithium–containing single–ion copolymer electrolytes **6** (black solid line) and **7** (red solid line) in D_2O, and **8** (black dashed line) and **9** (red dashed line) in DMSO–d_6.

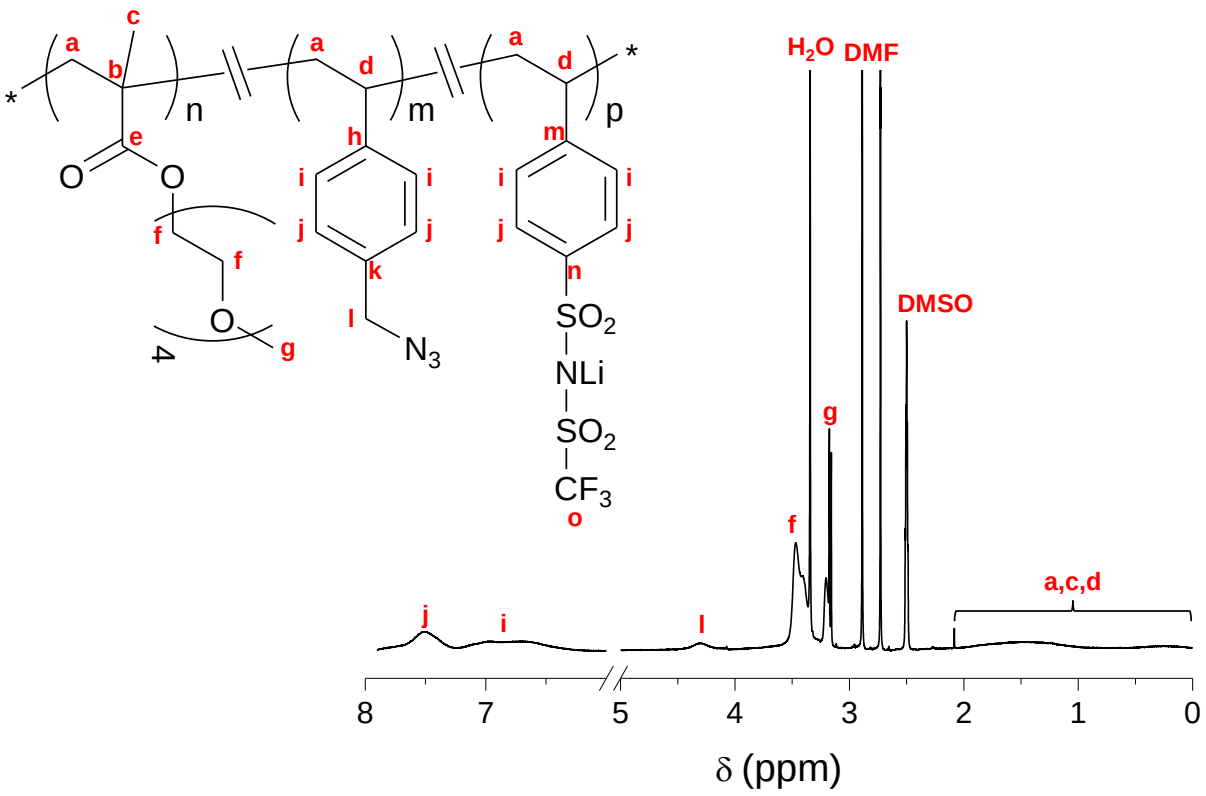

Figure S7. ^{1}H NMR of lithium–containing single–ion copolymer electrolyte **8** in DMSO-d_6.

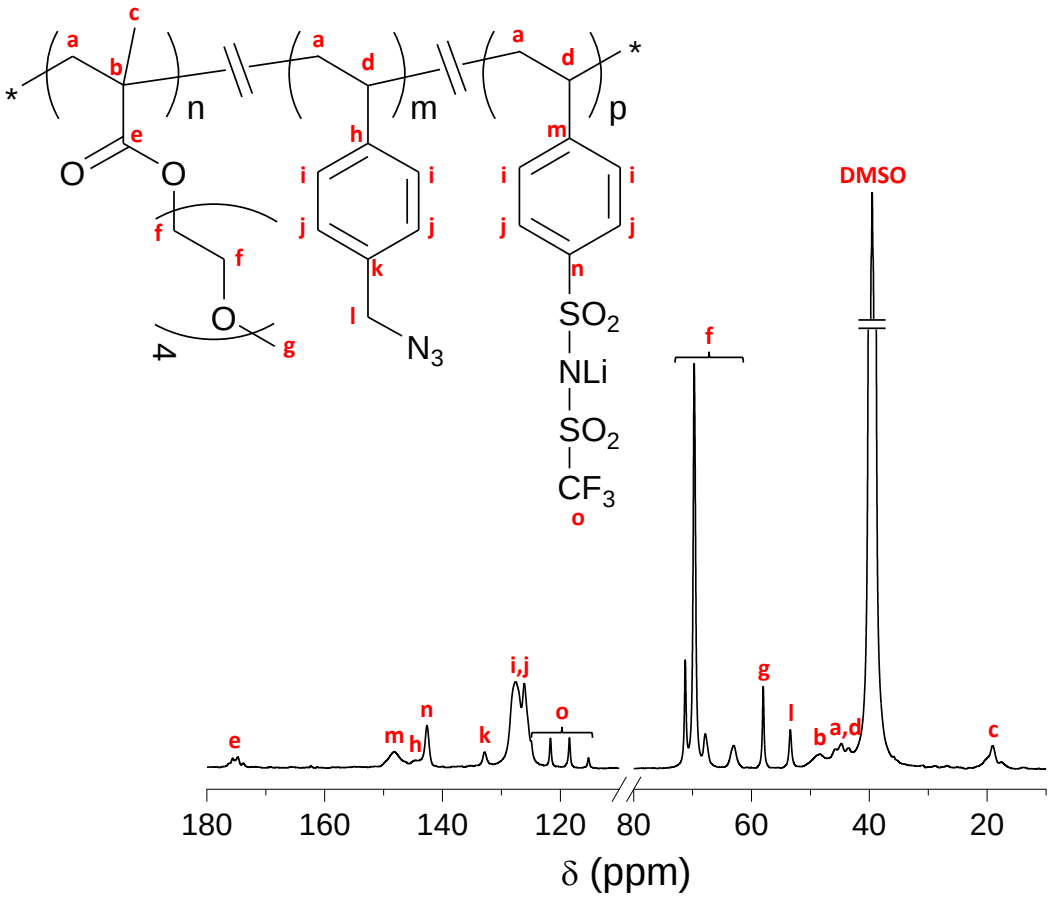

Figure S8. ^{13}C NMR of lithium–containing single–ion copolymer electrolyte **8** in DMSO-d_6.

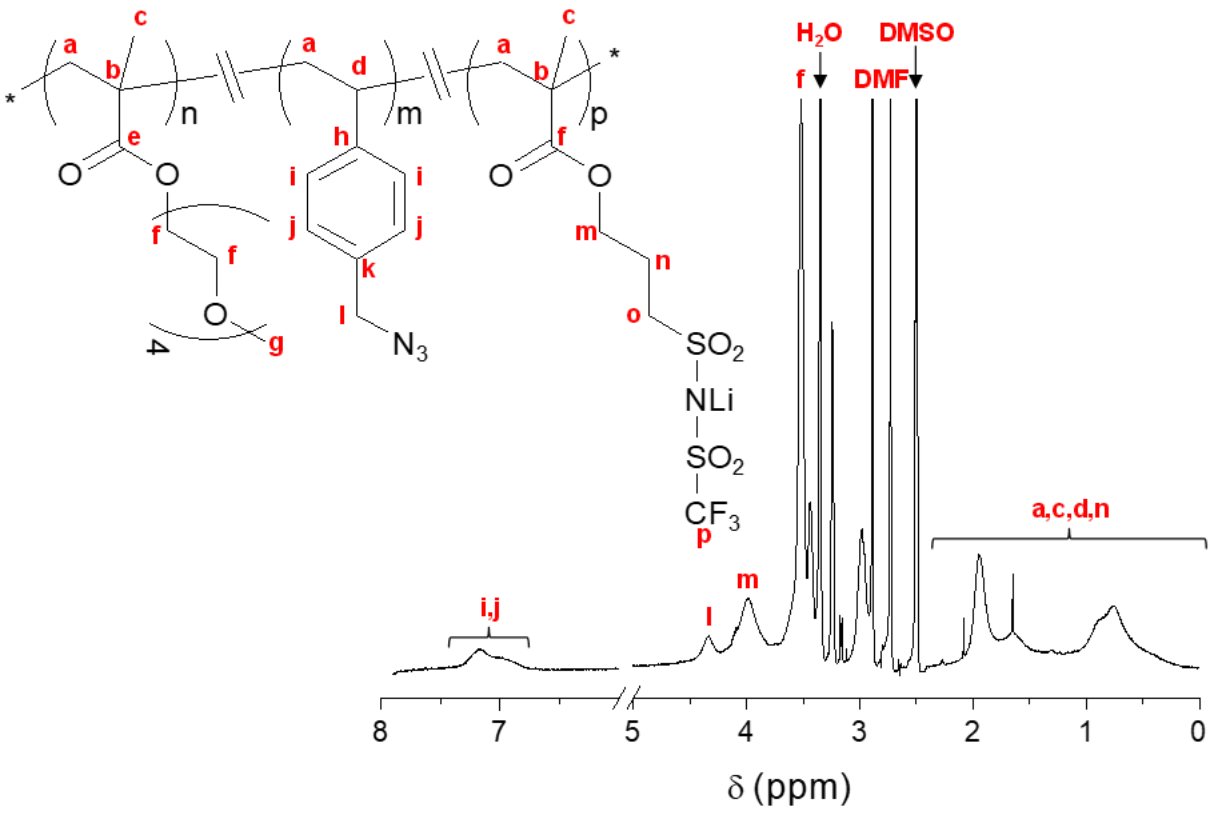

Figure S9. [1]H NMR of lithium–containing single–ion copolymer electrolyte **9** in DMSO-d_6.

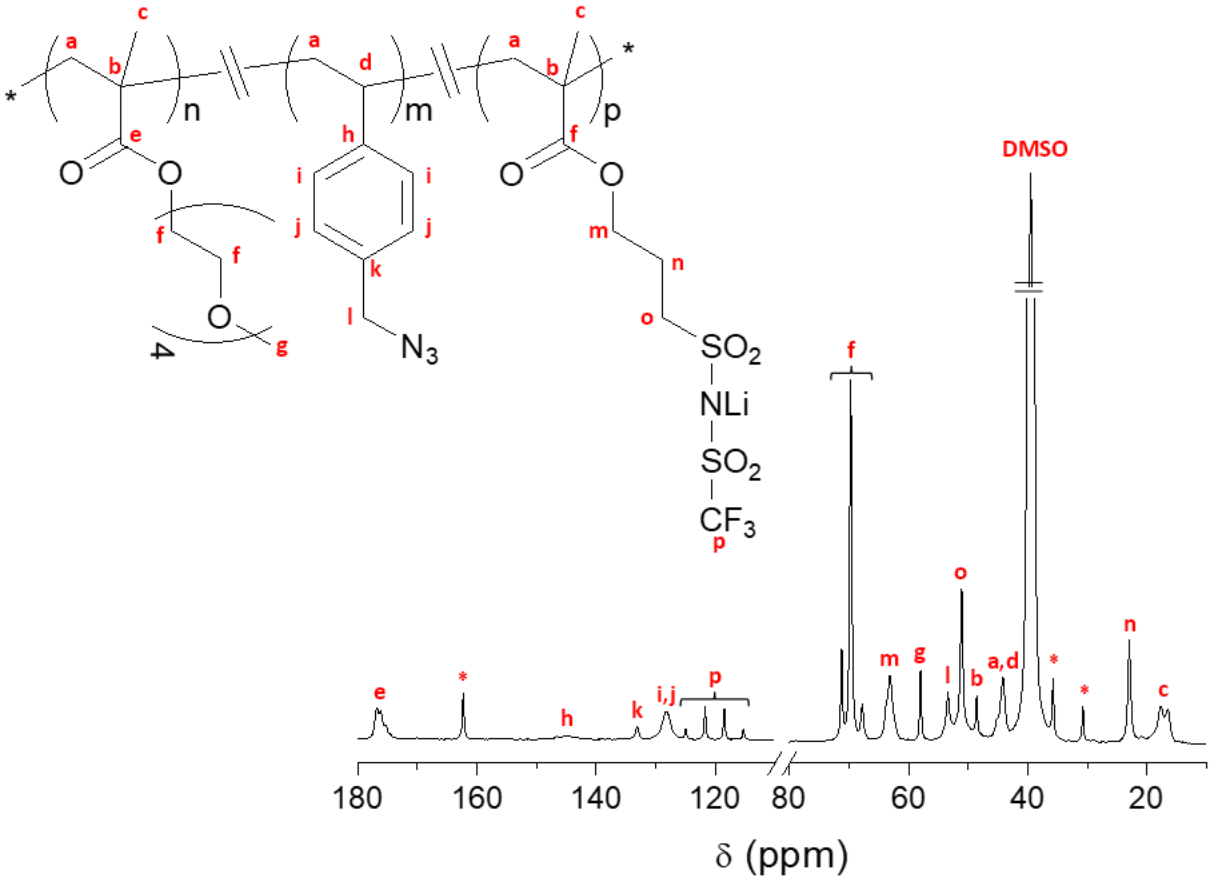

Figure S10. [13]C NMR of lithium–containing single–ion copolymer electrolyte **9** in DMSO-d_6.

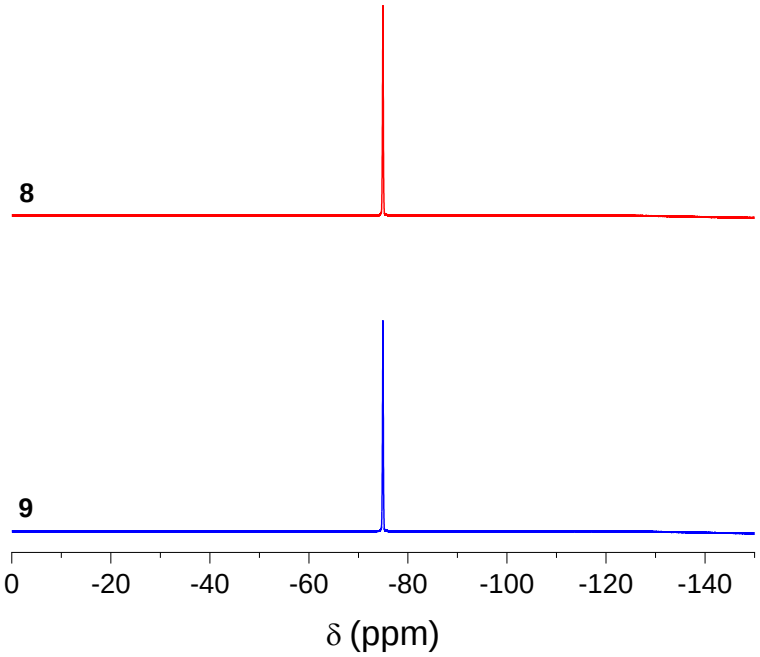

Figure S11. ^{19}F NMR of lithium–containing single–ion copolymer electrolytes **8** (black line) and **9** (red line) in DMSO-d_6.

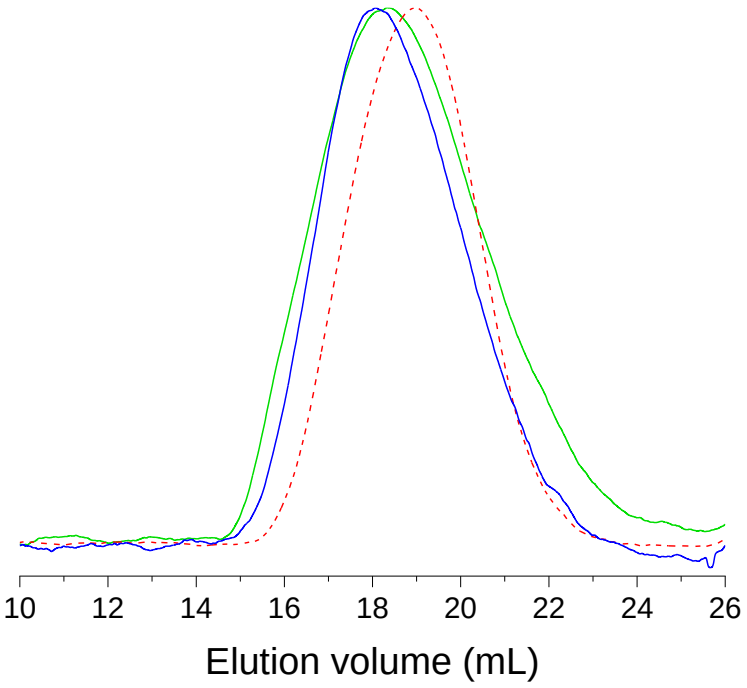

Figure S12. SEC traces (DMSO, 65 °C) of lithium–containing single–ion copolymer electrolytes **7** (black solid line), **8** (black dashed line) and **9** (red solid line).

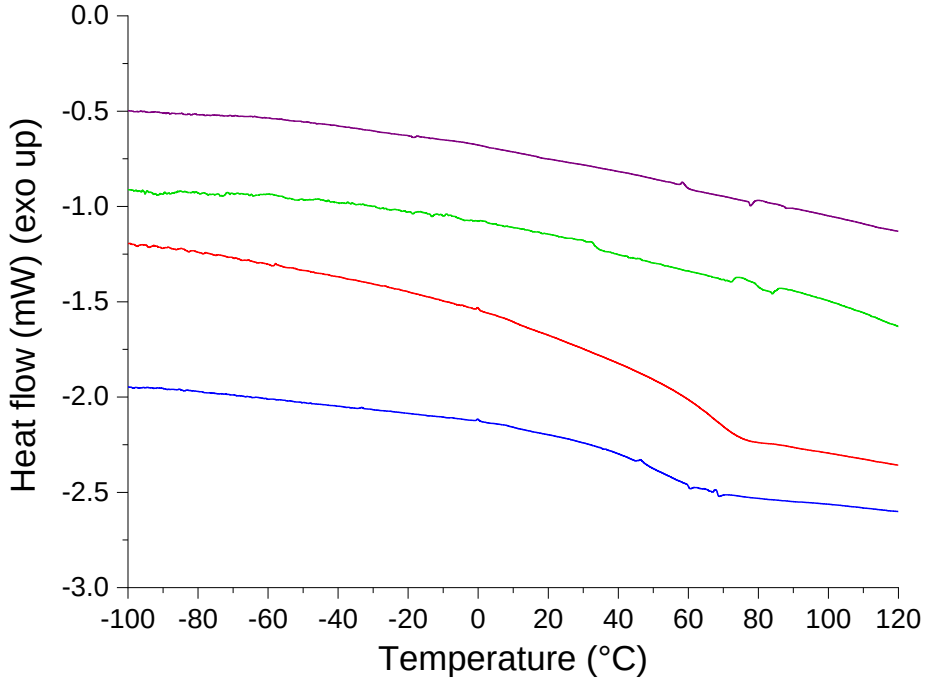

Figure S13. DSC traces of lithium–containing single–ion copolymer electrolytes **6** (black solid line), **7** (red solid line), **8** (black dashed line) and **9** (red dashed line).

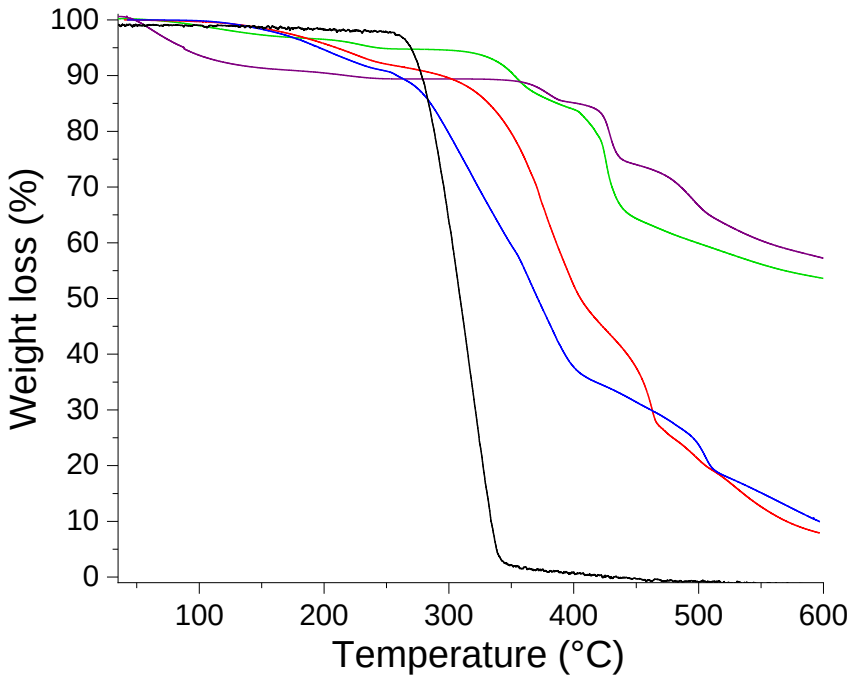

Figure S14. TGA traces of lithium–containing single–ion copolymer electrolytes **6** (purple solid line), **7** (green solid line), **8** (red solid line), **9** (blue solid line) and **C2400** separator (black solid line).

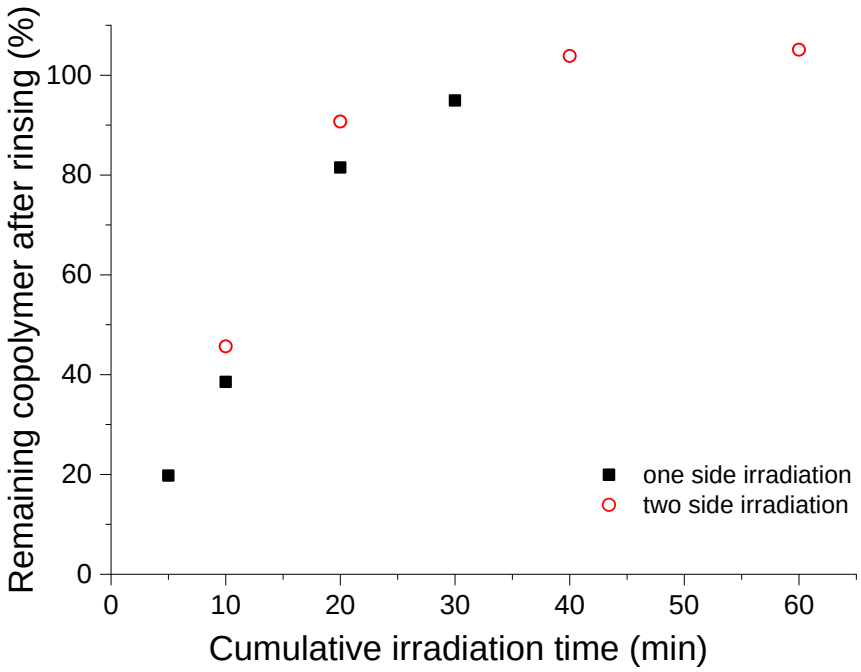

Figure S15. Kinetic study of the UV cross-linking of copolymer **8** on the surface of the pores of the **C2400** separator.

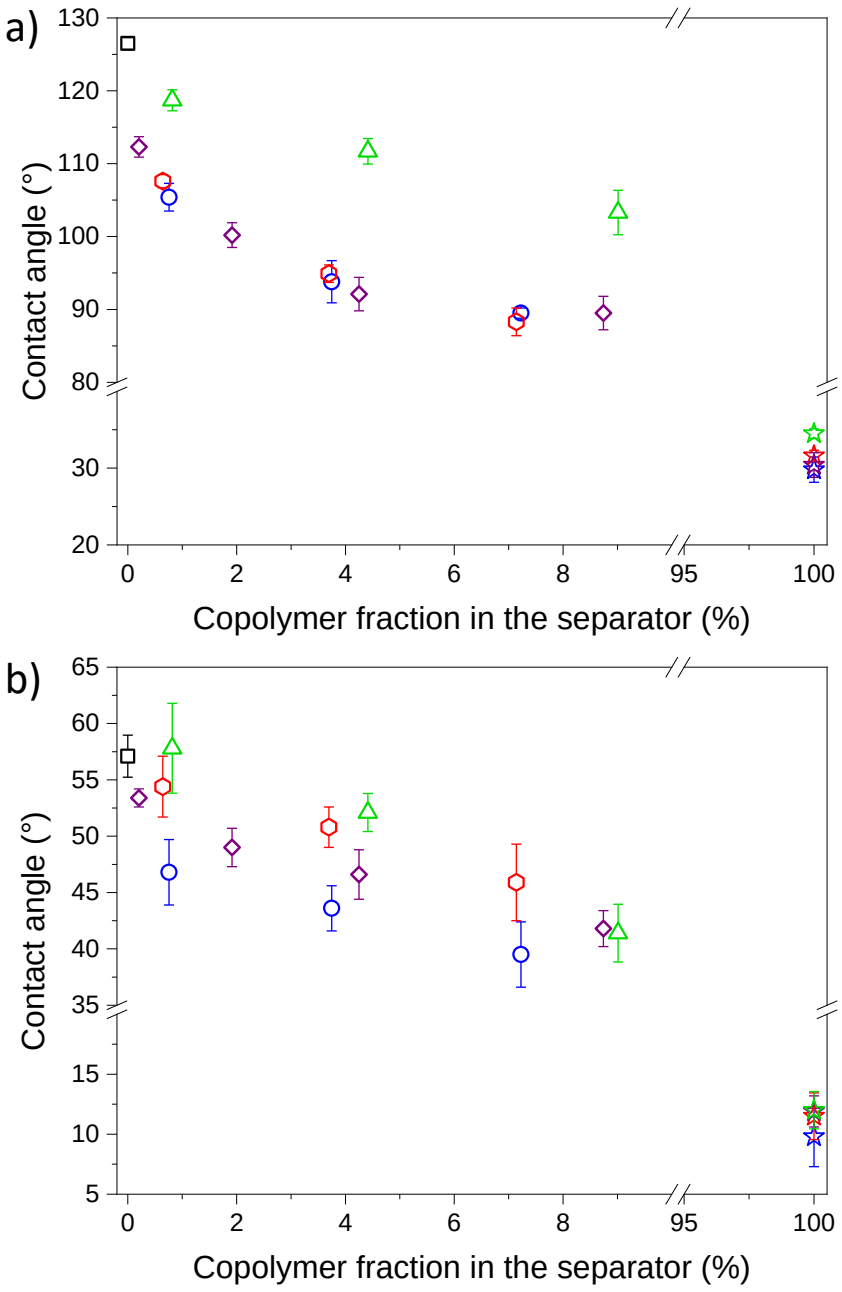

Figure S16. Contact angle of a) water and b) a 1:1 (vol/vol) EC/DMC mixture on **C2400** separator (open black squares), on functionalized separators **C6** (open purple diamonds), **C7** (open green triangles), **C8** (open red hexagons) and **C9** (open blue circles) for different contents of deposited copolymers **6**-**9**, and on ca. 60 nm thick cross-linked layers of copolymers **6** (open purple star), **7** (open green star), **8** (open red star) and **9** (open blue star) spin coated on silicon wafers.

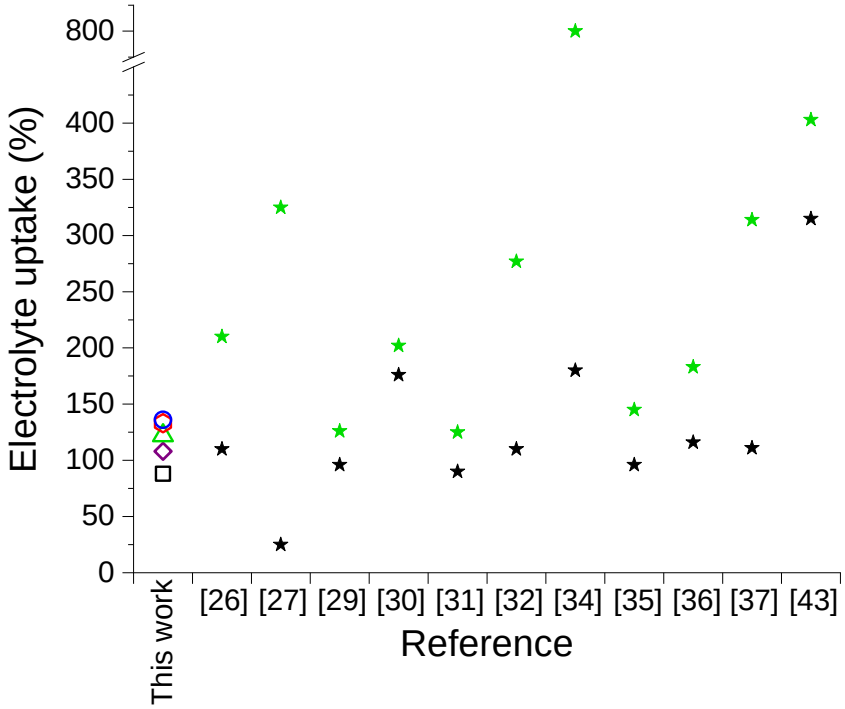

Figure S17. Electrolyte uptake of **C2400** separator (solid blue star), functionalized separators **C6** (open purple diamond), **C7** (open green triangle), **C8** (open red hexagon) and **C9** (open blue circle), and bare polyolefin separators (solid black stars) and corresponding functionalized separators (solid green stars) from literature. For more details on literature data see **Table S1**.

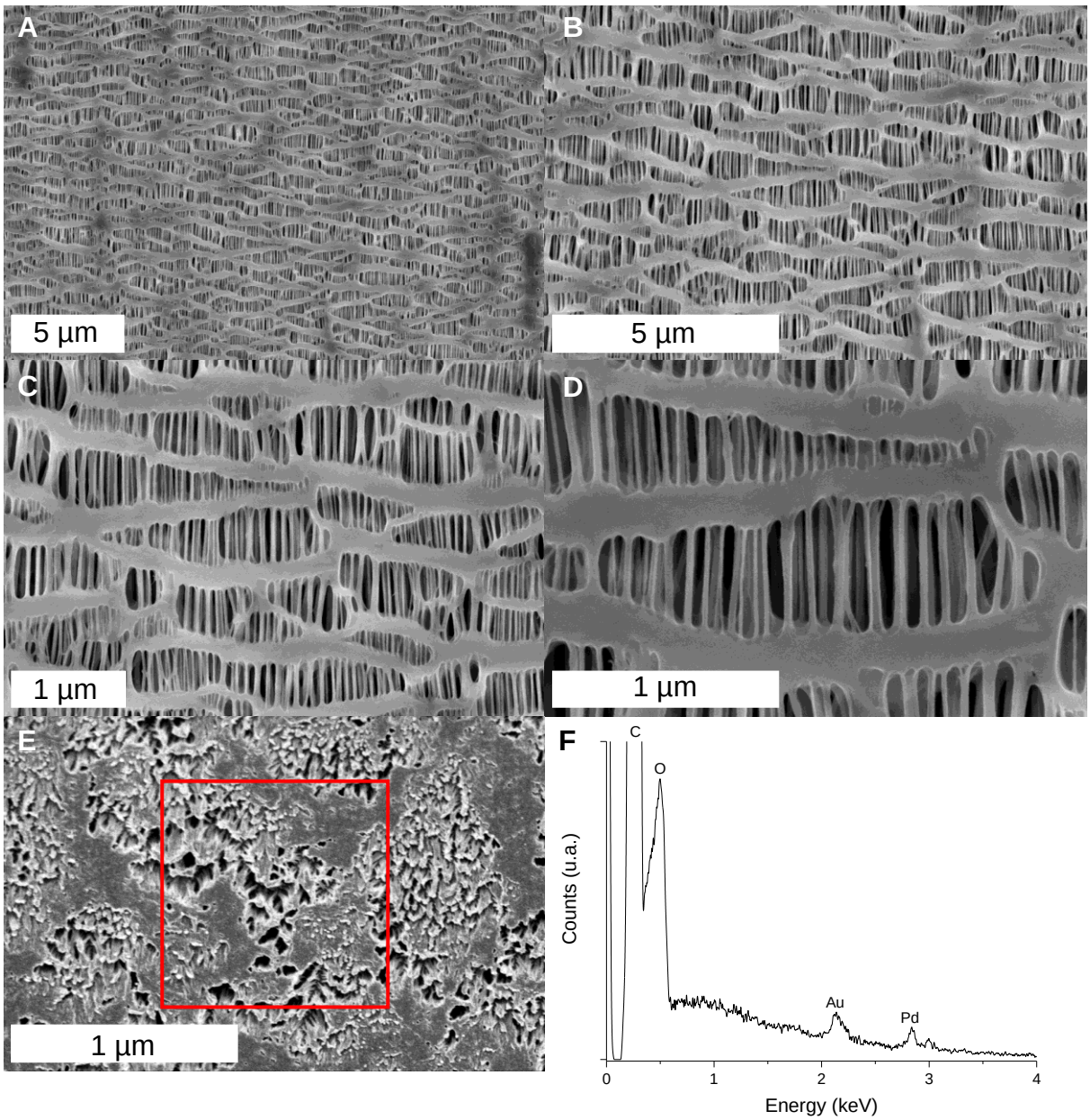

Figure S18. Scanning electron microscopy of the surface (A-D), cross-section (E), and SEM/EDX microanalysis (F) of the **C2400** separator. The red square in (E) represents the scanned area by SEM/EDX in (F).

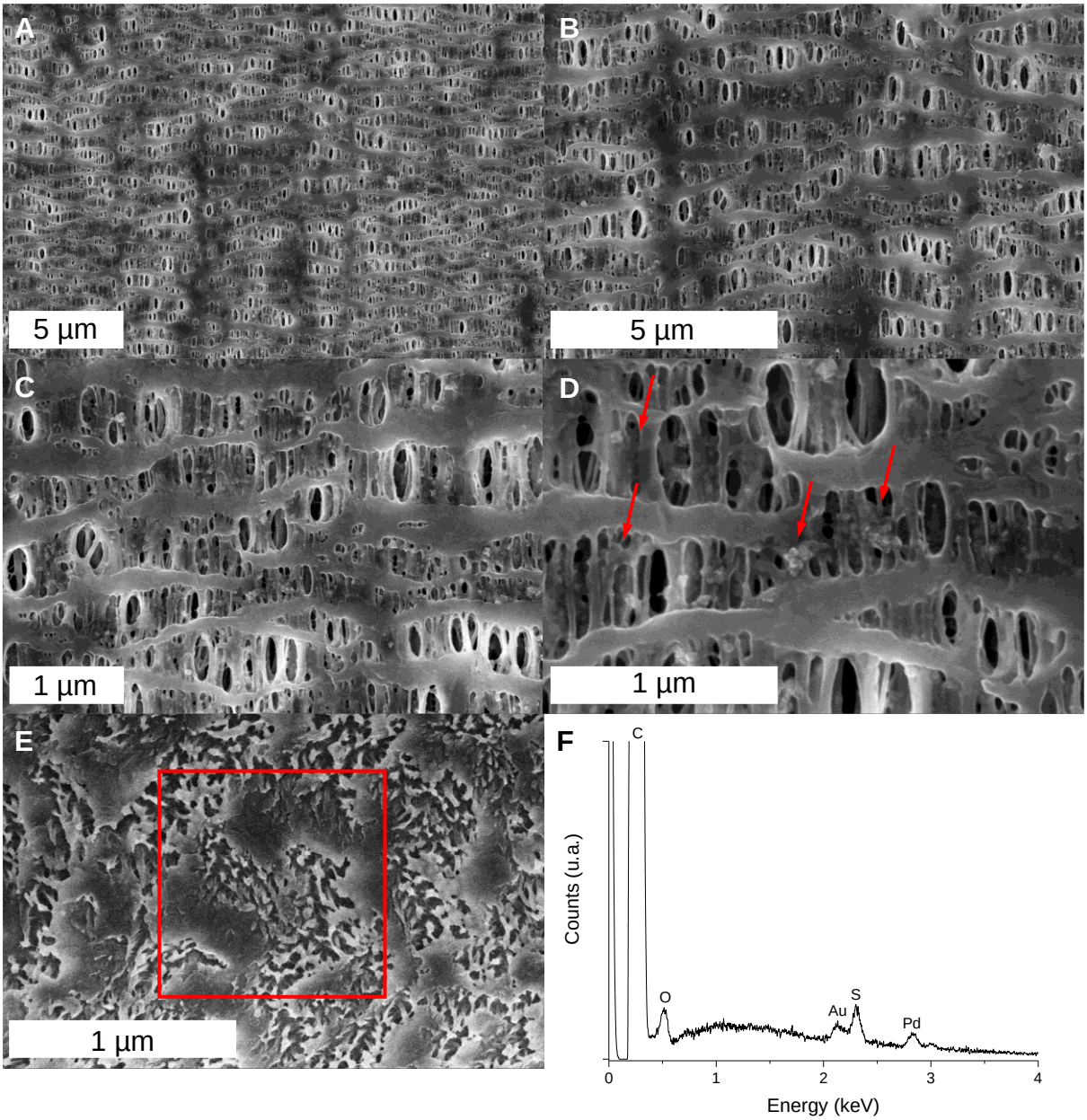

Figure S19. Scanning electron microscopy of the surface (A-D), cross-section (E), and SEM/EDX microanalysis (F) of functionalized separator **C6**. The red arrows in (D) highlight the presence of spherical aggregates and aggregated fibrils. The red square in (E) represents the scanned area by SEM/EDX in (F).

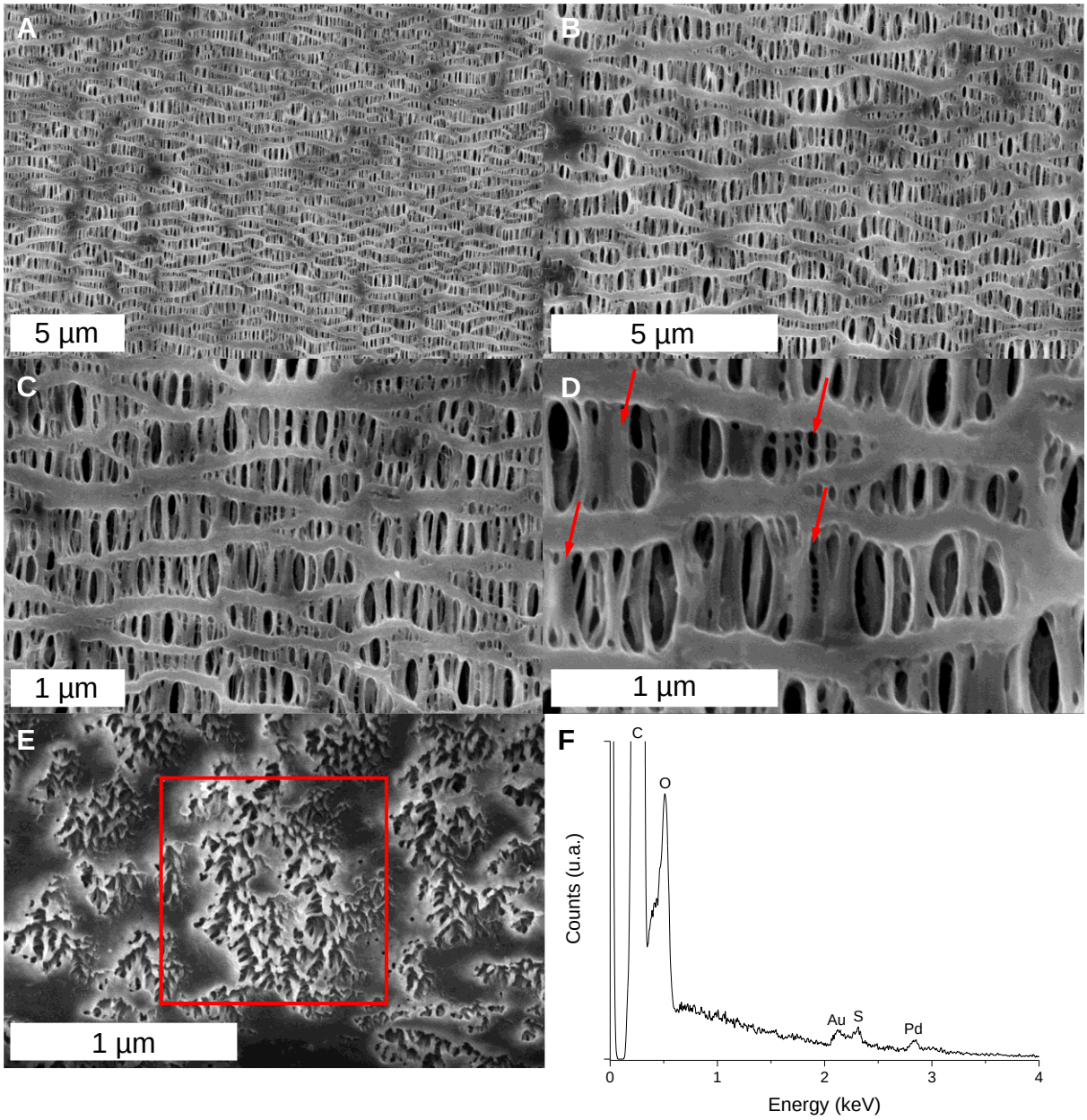

Figure S20. Scanning electron microscopy of the surface (A-D), cross-section (E), and SEM/EDX microanalysis (F) of functionalized separator **C7**. The red arrows in (D) highlight the presence of aggregated fibrils and perpendicular microfibrils. The red square in (E) represents the scanned area by SEM/EDX in (F).

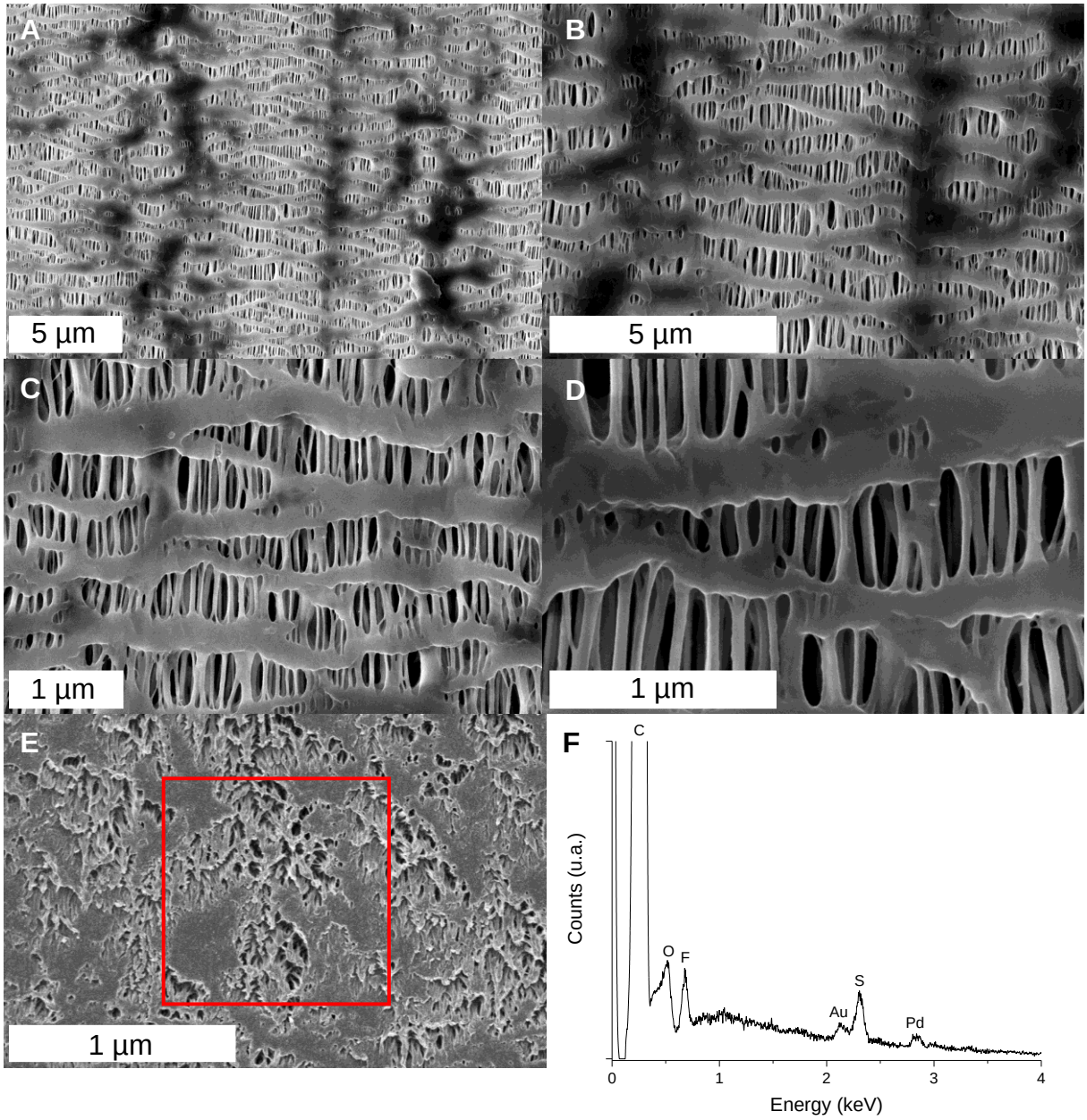

Figure S21. Scanning electron microscopy of the surface (A-D), cross-section (E), and SEM/EDX microanalysis (F) of functionalized separator **C8**. The red square in (E) represents the scanned area by SEM/EDX in (F).

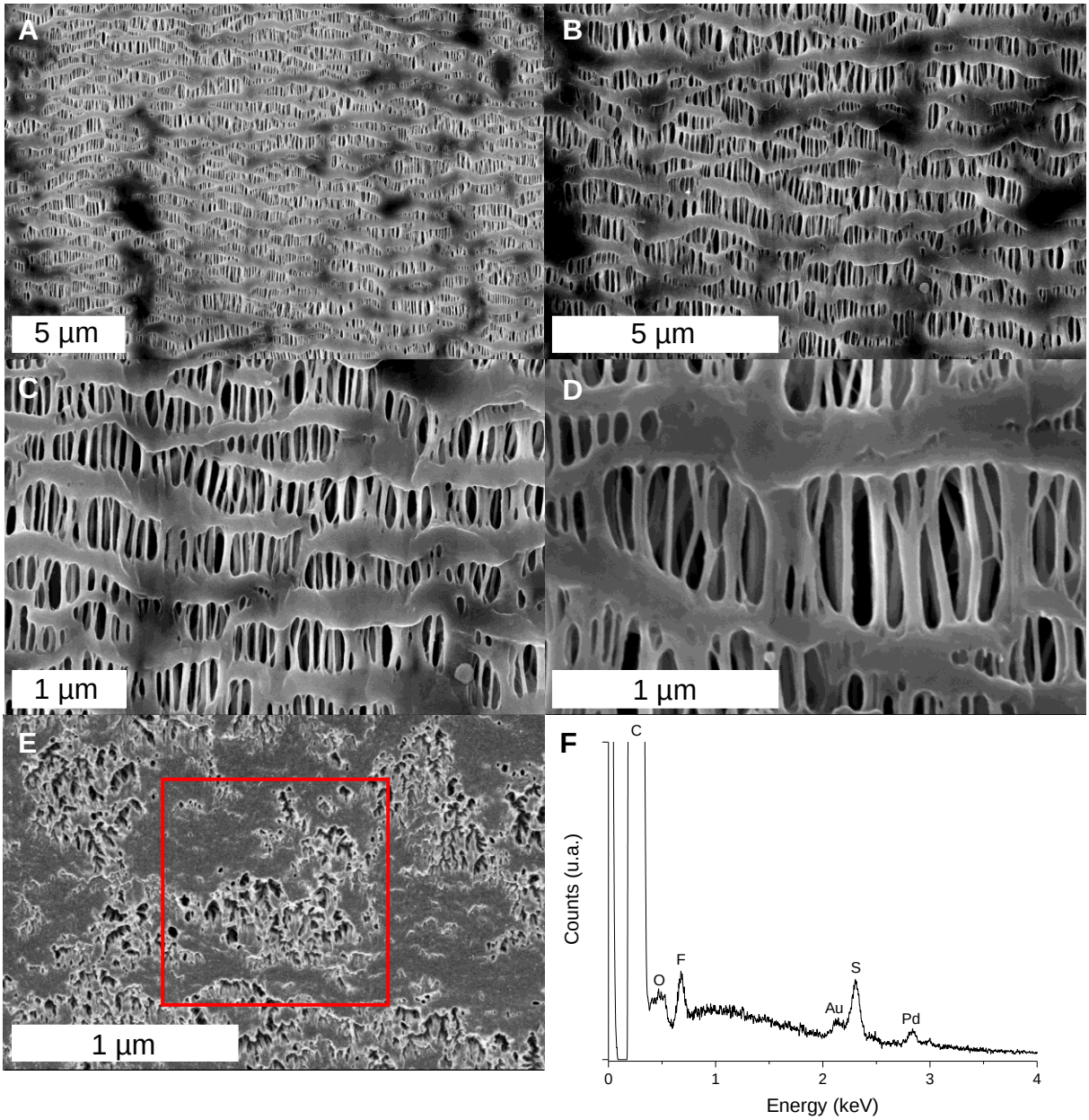

Figure S22. Scanning electron microscopy of the surface (A-D), cross-section (E), and SEM/EDX microanalysis (F) of functionalized separator **C9**. The red square in (E) represents the scanned area by SEM/EDX in (F).

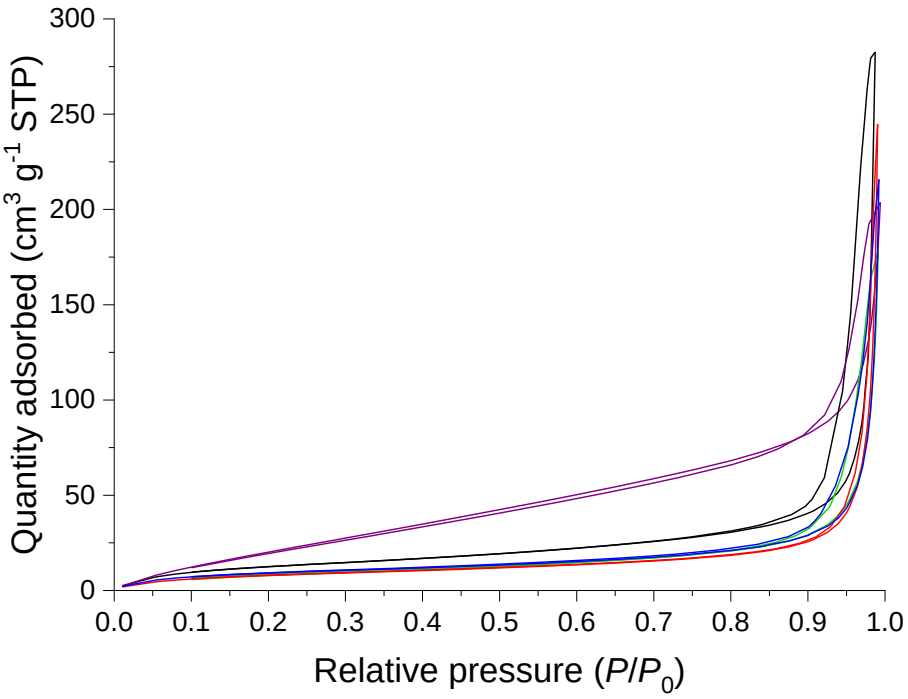

Figure S23. N_2 adsorption/desorption isotherms of a **C2400** separator (black solid line) and functionalized separators **C6** (purple solid line), **C7** (green solid line), **C8** (red solid line) and **C9** (blue solid line).

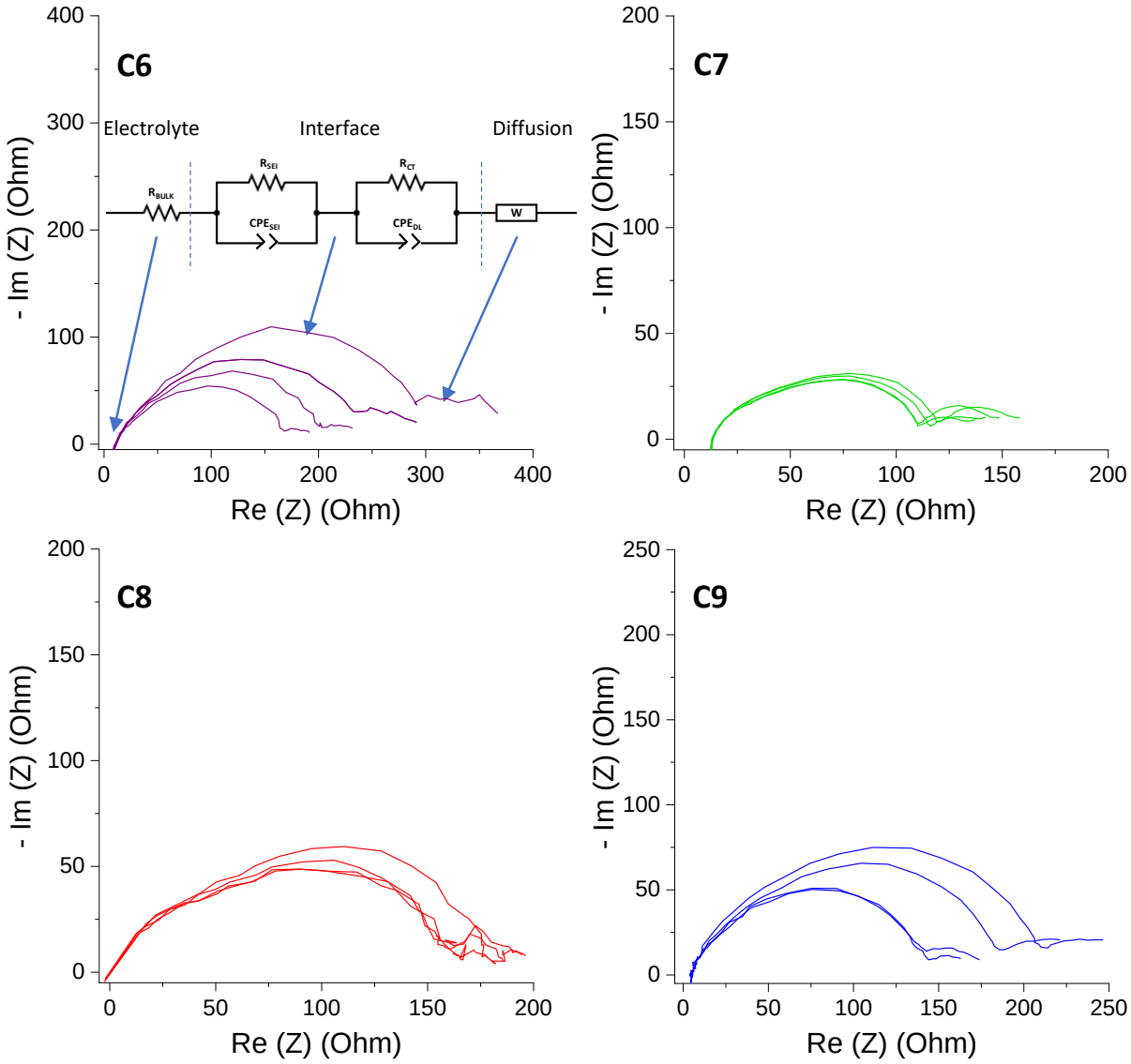

Figure S24. Nyquist diagrams during chronopotentiometry measurement of Li/Li symmetric cells using functionalized separators **C6**-**C9** soaked with LP30.

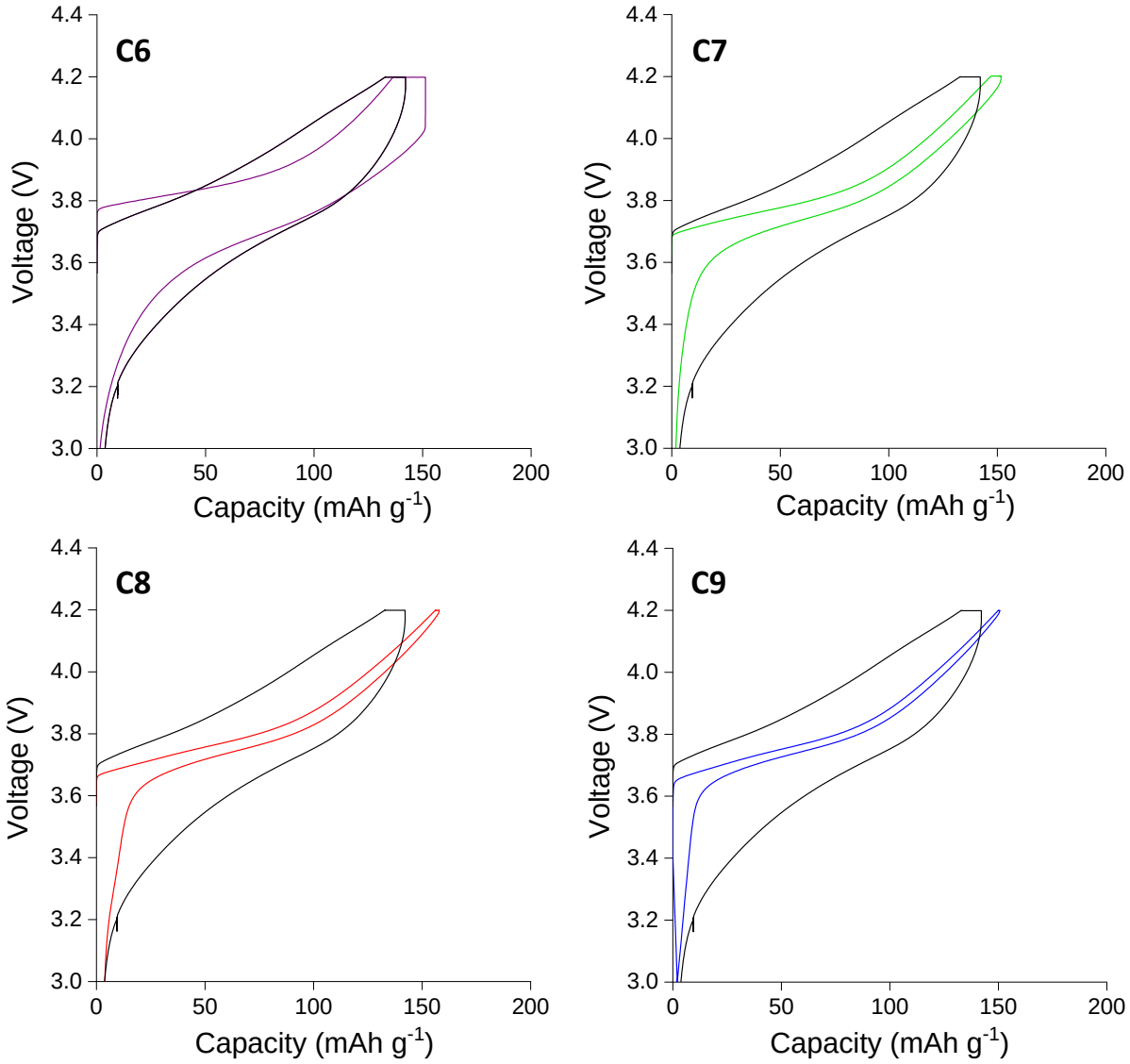

Figure S25. Charge-discharge profiles at 25 °C for the third cycle of galvanostatic cycling at *C*/10 (±200 μA cm^{-2}) of Li/NMC622 cells using the **C2400** separator (black solid lines) or functionalized separators **C6** (purple solid line), **C7** (green solid line), **C8** (red solid line) and **C9** (blue solid line).